

#### Contents lists available at ScienceDirect

### Materialia

journal homepage: www.elsevier.com/locate/mtla



#### Full Length Article

## Low temperature growth of Cu thin films on TiN(001) templates: Structure and energetics



Xiaoman Zhang<sup>a</sup>, Shuai Shao<sup>b</sup>, A.S.M. Miraz<sup>c</sup>, C.D. Wick<sup>c</sup>, B.R. Ramachandran<sup>d</sup>, W.J. Meng<sup>a,\*</sup>

- <sup>a</sup> Department of Mechanical & Industrial Engineering, Louisiana State University, Baton Rouge, LA 70803, USA
- b Department of Mechanical Engineering and the National Center for Additive Manufacturing Excellence, Auburn University, Auburn, AL 36849, USA
- <sup>c</sup> College of Engineering & Science, Louisiana Tech University, Ruston, LA 71272, USA
- <sup>d</sup> Institute for Micromanufacturing, Louisiana Tech University, Ruston, LA 71272, USA

#### ARTICLE INFO

# Keywords: Epitaxial growth Metal/ceramic interfaces Orientation relationship Modified embedded atom method potentials Interfacial energetics

#### ABSTRACT

Synthesis of metal/ceramic interfaces with well-defined structural characteristics is an important step toward understanding the energetics and mechanical response of such interfaces. We used ultra-high-vacuum magnetron sputter deposition to grow elemental Cu thin films onto single crystal TiN(001) thin film templates, grown heteroepitaxially onto single crystal MgO(001) substrates. Structure of the Cu thin films grown on TiN(001) templates was examined as a function of the growth temperature. At close to room temperature, we observed the previously reported cube-on-cube orientation relationship between Cu and TiN, with Cu(001)//TiN(001). At a slightly elevated temperature, we observed a new Cu-TiN orientation relationship with Cu(110)//TiN(001) that, to the best of our knowledge, is reported here for the first time. Accompanying molecular dynamics simulations with modified embedded atom method potentials newly developed for the Cu-TiN system showed the influence of nanoscale twinning and lattice strain on structure and interfacial energetics of Cu/TiN bicrystals. Controlled growth of metal/ceramic bicrystal thin films offers an opportunity for systematic testing of the mechanical response of metal/ceramic interfaces with better defined structural characteristics.

#### 1. Introduction

Metal/ceramic interfaces are relevant to wide ranging engineering materials and applications, examples of which include cermets for molds and cutting tools [1], functional devices such as sensors and actuators [2], and mechanical components such as valve seats and guides [3]. Achieving a detailed understanding of the energetics and mechanical responses of metal/ceramic interfaces is key to effective design and implementation of mechanical applications in which performance is critically influenced by the presence of such interfaces.

Cu/MgO bicrystals have served as a model system for studying metal/ceramic interfaces [4]. With the bulk lattice parameters of  $a_{\rm MgO}=4.21$  Å and  $a_{\rm Cu}=3.61$  Å, the Cu/MgO system possesses a large lattice mismatch,  $(a_{\rm Cu}-a_{\rm MgO})/a_{\rm MgO}=-0.1425$ . Despite this, Cu thin films can be grown heteroepitaxially on MgO substrates by ultra-high-vacuum (UHV) vapor phase growth, usually reported in the "cube-oncube" orientation with Cu(001)//MgO(001) and Cu[100]//MgO[100] [5, 6]. TiN is isostructural with MgO, and a prototypical example of rocksalt structured refractory transition metal nitrides [7]. Growth of TiN thin films has been studied for understanding of basic vapor phase growth behavior of ceramics [8]. Structure and mechanical response of

interfaces between various metals and TiN are of interest for fundamental understanding and relevant to surface engineering applications [9, 10].

Quantitative measurements of the mechanical response of metal/ceramic interfacial regions have remained a challenge over the past two decades. To this end, advances in nano/micro scale machining with focused ion beam (FIB) [11] have enabled direct mechanical loading and quantitative measurement of the response of metal/ceramic interfacial regions in FIB-milled microscale specimens under simple loading conditions, such as shear, compression, and tension [12, 13, 14]. However, these preliminary microscale mechanical tests were conducted on interfaces between nanocrystalline metals and ceramics. The structural complexity of such interfaces complicates interpretation of the testing data. Paralleling experimental advances, density functional theory (DFT) calculations and molecular dynamics (MD) simulations have increasingly been used to obtain energetics as well as tension and shear response of metal/ceramic interfaces [1, 2, 13, 15, 16, 17]. Even with the phenomenal increase in computing power over the last two decades, present DFT and MD simulations are still computationally limited to simple interface geometries, e.g., DFT calculations are limited to coherent or completely incoherent interface

E-mail address: wmeng1@lsu.edu (W.J. Meng).

<sup>\*</sup> Corresponding author.

structures, and MD simulations are limited to structures whose volume is smaller than 50 nm  $\times$  50 nm  $\times$  50 nm (about 15 $\sim$ 20 million atoms) [18, 19]. Thus, synthesis of metal/ceramic interfaces with structural characteristics better defined than those between nanocrystalline metals and ceramics is motivated by the desire to yield mechanical response data on simpler metal/ceramic interfaces, and thus facilitate more direct comparison between experimental results and those from DFT and MD simulations.

The bulk lattice parameter of TiN,  $a_{\rm TiN} = 4.24$  Å, is closely matched to that of MgO,  $\delta = (a_{\rm TiN} - a_{\rm MgO})/a_{\rm MgO} = +0.007$ , allowing heteroepitaxial growth of TiN thin films on MgO(001) substrates in the cube-on-cube orientation [20]. Epitaxial TiN(001) thin films grown on MgO(001) have also been used as a growth template for Cu thin films [21]. In the present paper, we report results of growth and structural characterization of Cu thin films on TiN(001) thin film templates, grown heteroepitaxially on MgO(001) substrates, as a function of the growth temperature. In addition to the observation of cube-on-cube Cu/TiN growth, a new Cu/TiN orientation relationship (OR) is observed with Cu(110)//TiN(001) in the growth direction, and Cu<111>//TiN<100> and Cu<112>//TiN<100> within the growth plane. To the best of our knowledge, this OR is being reported here for the first time. Molecular dynamics simulations utilizing modified embedded atom method (MEAM) potentials for the Cu-TiN system, newly developed by the present authors, were performed in an attempt to rationalize the present experimental observations.

#### 2. Procedures for experimentation and computation

#### 2.1. Experimental procedures

Two-side polished MgO(001) wafers (99.99%), with dimensions of  $10 \times 10 \times 0.5$  mm³, were cleaned with successive rinses in ultrasonic baths of acetone, ethanol, and deionized water, and blown dry with dry  $N_2$ . Cleaned MgO substrates were mounted with one side covered in an aluminum holder and loaded into a high vacuum chamber with base pressure  $< 3 \times 10^{-8}$  Torr. The exposed side of the MgO substrate was then etched in an Ar (99.999%+) inductively coupled plasma (ICP) for  $\sim$ 5 min at a  $\sim$ 50 V bias to the aluminum holder, followed by elemental Si (99.95%) deposition from a 7.5 cm diameter Si magnetron sputter source in pure Ar without intentional heating. The thickness of the deposited Si layer was  $\sim$ 1  $\mu$ m.

The one-side Si-deposited MgO(001) wafer was unloaded from the high vacuum system, cleaned again with acetone and ethanol, dried with dry N2, mounted onto a molybdenum holder, and inserted into a load-lock chamber for transport into an UHV dc magnetron sputter deposition chamber with a base pressure of  $\sim 1 \times 10^{-9}$  Torr. The deposition chamber houses two 7.5 cm diameter Ti (99.95%) magnetron sputter sources, one 7.5 cm diameter Cu (99.99%) magnetron sputter source, and a high temperature substrate stage with radiation heating from SiC heating elements. The Si-deposited side of the MgO wafer faced the heating elements and the not-deposited side of the MgO wafer faced the incoming vapor flux. The actual substrate temperature was determined by measuring the temperature of a pristine Si wafer mounted onto the same molybdenum holder through direct optical access infrared pyrometry, with the Si wafer emissivity set at 0.68. Substrate temperature monitoring was accomplished by a separate thermocouple placed in close proximity to the molybdenum holder. A substrate temperature calibration curve was established by conducting multiple measurements of the Si wafer temperature with the infrared pyrometer, while conducting simultaneous thermocouple temperature readings. During growth onto backside-Si-deposited MgO(001) wafers, the deposition temperature was determined from the thermocouple reading, cross referenced to the temperature calibration curve.

The MgO(001) wafers were thermally degassed in the UHV deposition chamber at 800  $^{\circ}$ C for 20 min. Sputter deposition of TiN commenced immediately after degassing at the same temperature, with the two Ti sources operating at a constant current of 1.35 A in an Ar/N<sub>2</sub> (99.999%)

mixture at a total pressure of  $\sim$ 4 mTorr, with a -40 V substrate bias voltage applied. The  $\rm N_2$  flow was adjusted to be close to the point of stoichiometric deposition. After the TiN deposition, the substrate temperature was decreased and equilibrated at temperatures varying from  $\sim$ 70 °C to  $\sim$ 250 °C. Sputter deposition of Cu commenced after temperature equilibration in pure Ar (99.999%) at a total pressure of  $\sim$ 4 mTorr, with no substrate bias voltage applied and the Cu source operating at a constant current of 1.35 A. After Cu deposition, the Cu/TiN/MgO(001) specimen was allowed to cool to close to room temperature before being transferred out of the deposition system. Cu/TiN/MgO(001) specimens were made at varying Cu top layer growth temperatures and with varying Cu top layer thicknesses, keeping the growth temperature of the TiN buffer layer fixed at 800 °C. Typical deposition rates for TiN and Cu are  $\sim$ 1.5 Å/sec and  $\sim$ 3 Å/sec, respectively.

The morphology, structure, and crystal quality of Cu/TiN/MgO(001)  $\,$ specimens were characterized by combining scanning electron microscopy (SEM) and Ga+ FIB sectioning, X-ray diffraction (XRD), and transmission electron microscopy (TEM). Scanning imaging with electron- or ion- induced secondary electrons (SEs/ISEs) and Ga+ FIB milling were carried out on an FEI Quanta3D Dual-Beam FEG instrument, which also housed an X-ray energy dispersive spectroscopy (EDS) attachment (EDAX), an electron backscatter diffraction (EBSD) attachment (EDAX), a Ga+ ion beam catalyzed organometallic Pt deposition attachment, and an OmniProbe attachment for site-selective specimen lift-out. X-ray  $\theta/2\theta$  scans,  $\omega$  rocking curve scans, asymmetric  $\phi$  scans, and reciprocal lattice mapping (RSM) were collected on a PANalytical Empyrean system. The incident Cu Kα X-ray was passed through a fourbounce Ge(220) monochromator, selecting the incident X-ray wavelength  $\lambda = 1.540598$  Å. The specimens were mounted on a  $\chi$ - $\phi$ -x-y-z stage. Scattering signals were collected by a PIXcel 3D detector. XRD data were analyzed with the PANalytical HighScore<sup>TM</sup> and Epitaxy<sup>TM</sup> software packages. A JEOL JEM2011 microscope operated at 200 kV was used for electron selected area diffraction (SAD) as well as brightfield/dark-field (BF/DF) imaging. Specimen preparation for TEM examinations proceeded with OmniProbe lift-out following standard procedures, followed by Ga+ ion milling in the SEM/FIB instrument, finished with low energy Ar+ ion polishing at 100 eV with a Gatan PIPS-II Precision Ion Polishing system.

#### 2.2. Computational procedures

MD simulations on Cu/TiN bicrystals were carried out using MEAM potentials [22, 23, 24, 25, 26, 27] developed by the present authors. The model was parameterized using a generic algorithm we developed in a previous work [28], and fitted to a combination of experimental properties and DFT results. For this work, most of the DFT results were carried out using the VASP simulation software [29]. Further details regarding the parameterization, along with the results of different property comparisons with experiment and DFT, are given in the Supplemental Materials Section S1. Additional MD simulations on Cu were carried out using a previously reported embedded atom method (EAM) potential [30].

Using the Cu-TiN MEAM potentials and the Cu EAM potential, four sets of simulations were performed:

- (1) Set 1: to assess the effect of nano-twin boundary spacing on the equilibrium lattice constant of Cu;
- (2) Set 2: to assess the effect of nano-twin boundary spacing on the linear thermal expansion of Cu;
- (3) Set 3: to assess the effect of in-plane strains experienced by the Cu layer on excess energies of Cu/TiN interfaces;
- (4) assess the effect of the location of misfit dislocation network (MDN) on the excess energy of the Cu/TiN interface.

Molecular dynamics/statics simulations were performed using the Large-scale Atomic/Molecular Massively Parallel Simulator (LAMMPS) [31]. The atomistic structures were visualized by the Open Visualization

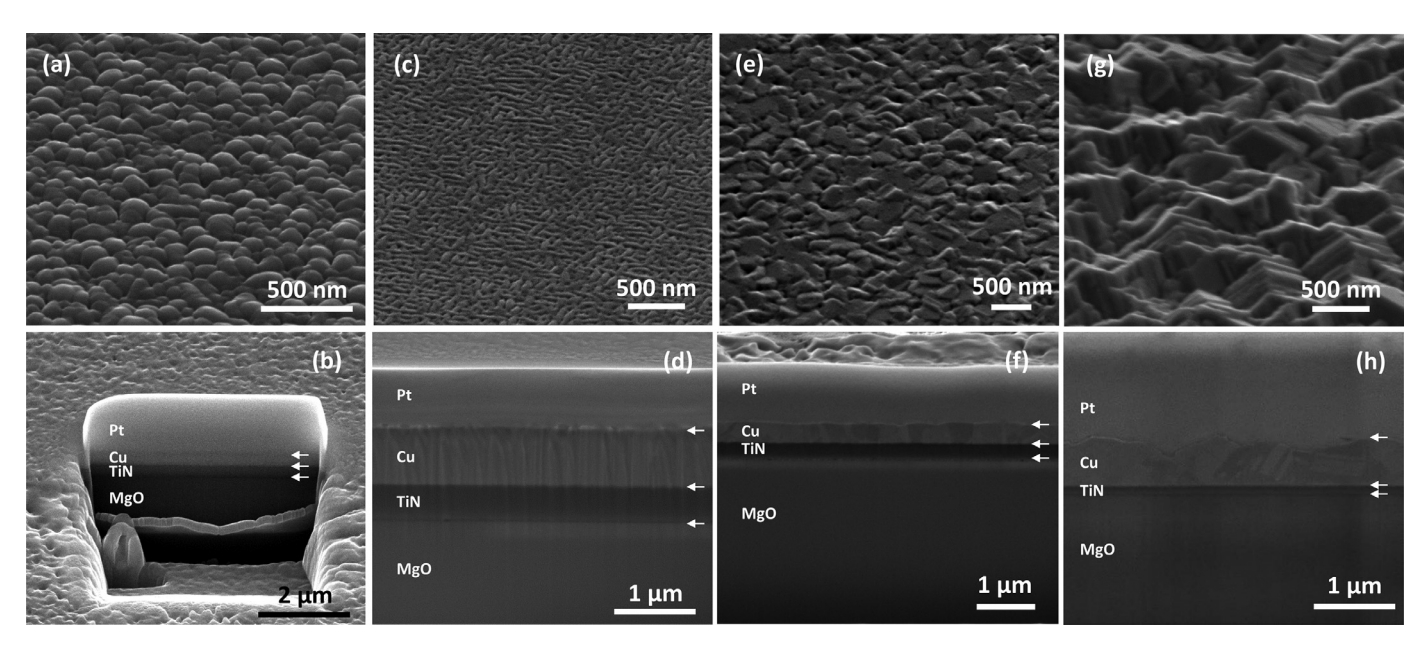


Fig. 1. Morphology of Cu layers in Cu/TiN bilayers: surface and cross-sectional secondary electron images of Cu layers grown at (a)/(b) 75 °C; (c)/(d) 105 °C; (e)/(f) 180 °C; (g)/(h) 250 °C. All surface images were taken at a 52° tilt angle. In all cross-sectional images, Pt was deposited onto the specimen surface prior to Ga<sup>+</sup> milling, and protected the Cu surface from ion beam damage, as shown more clearly in the lower magnification view of (b). The white arrows mark locations of various interfaces.

Tool [32]. Further simulation details are supplied in the Supplemental Materials Section S2.

#### 3. Results and discussion

Fig. 1 shows the morphology of Cu layers in Cu/TiN bilayer specimens on MgO(001) substrates as a function of the Cu growth temperature. At 75 °C, Fig. 1(a) shows that the Cu top layer appears to be dense but its surface rough and "bumpy", with the bumps appearing to be isotropic. Fig. 1(b) shows the corresponding Ga+ FIB cross sectional view. The TiN buffer layer and the Cu top layer appear dense and uniform in thickness and contrast. The Cu layer thickness is ~355 nm. At 105 °C, Fig. 1(c) shows a lenticular morphology of the Cu top layer surface, different from the "bumpy" surface shown in Fig. 1(a) and smoother in comparison. The two groups of elongated lenticular shapes appear to be perpendicular to each other. Fig. 1(d) shows the corresponding Ga+ FIB cross sectional view. Again, the TiN buffer layer and the Cu top layer appear dense and uniform in thickness and contrast. The Cu layer thickness is ~730 nm. The top surfaces of Cu layers grown at 180 °C and 250 °C, shown respectively in Fig. 1(e) and 1(g), display significant faceting and increased roughness. The corresponding Ga+ FIB cross sectional views, shown respectively in Fig. 1(f) and 1(h), echo the increased roughness and further display contrasts typical of polycrystalline films.

Fig. 2 documents changes in Cu/TiN bilayer specimens on MgO(001) substrates as the Cu growth temperature increases from 75 °C to 105 °C, as shown by results of XRD characterization. At 75 °C, the symmetric  $\theta/2\theta$  scan, shown in Fig. 2(a), shows the presence of MgO (002) and (004) reflections, TiN (002) and (004) reflections, and the Cu (002) reflection, indicating complete texture of the TiN buffer layer and the Cu top layer, with Cu[001]//TiN[001]//MgO[001]. Fig. 2(b) shows the corresponding asymmetric 360°  $\phi$  scans for the (024) reflections of MgO, TiN, and Cu. Four peaks at 90° intervals are observed in each case, consistent with the cubic crystal structure of MgO, TiN, and Cu. Peaks for MgO, TiN, and Cu are completely aligned in  $\phi$ , indicating that both the TiN buffer layer and the Cu top layer were grown epitaxially onto the MgO(001) substrate in the cube-on-cube orientation, with Cu(001)//TiN(001)//MgO(001), and Cu[100]//TiN[100]//MgO[100].

The cube-on-cube OR between Cu and TiN is denoted as OR1. Fig. 2(c) shows the corresponding  $\omega$  rocking curve scans on (002) reflections of MgO, TiN, and Cu. The full-width-at-half-maximum (FWHM) of the three  $\omega$  rocking curves are respectively  $\sim$ 0.06°,  $\sim$ 0.49°, and  $\sim$ 1.47°. Data shown in Fig. 2(a), 2(b), and 2(c) establish Cu growth on TiN(001) template in the cube-on-cube orientation at 75 °C, consistent with previous studies [21].

At 105 °C, the symmetric  $\theta/2\theta$  scan, shown in Fig. 2(d), shows the presence of MgO (002) and (004) reflections, TiN (002) and (004) reflections, and the Cu (220) reflection. Data shown in Fig. 2(d) again indicate complete texture of the TiN buffer, TiN[001]//MgO[001]. The corresponding asymmetric 360°  $\phi$  scans for the (024) reflections of MgO and TiN and (402) reflection of Cu are shown in Fig. 2(e). Four (024) peaks are again observed at 90° intervals for MgO and TiN, with complete alignment. This indicates that the TiN buffer layer was again grown epitaxially onto the MgO(001) substrate in the cube-on-cube orientation, with TiN(001)//MgO(001) and TiN[100]//MgO[100]. In contrast, data shown in Fig. 2(d) and 2(e) show one significant difference from the 75 °C Cu growth case documented in Fig. 2(a-c), in that a complete but different texture is observed for the Cu top layer grown at 105 °C, with Cu[110]//MgO[001]. In addition, Fig. 2(e) demonstrates the presence of a different in-plane alignment for the Cu top layer grown at 105 °C: the  $\phi$  scan on the Cu (402) reflection shows a group of three peaks repeating at 90° intervals: the middle peak is aligned with TiN and MgO (024) peaks while the other two are on either side of the middle peak with a spacing of  $\sim 19.6^{\circ}$ . Fig. 2(f) shows corresponding  $\omega$  rocking curve scans on (002) reflections of MgO and TiN, and that on the (220) reflection of Cu. The FWHM of the three  $\omega$  rocking curves are respectively  $\sim 0.02^{\circ}$ ,  $\sim 0.2^{\circ}$ , and  $\sim 0.4^{\circ}$ .

The XRD data shown in Fig. 2(d) and 2(e) signify, to the best of our knowledge, a new orientation relationship between the Cu top layer and the TiN buffer layer that has not been reported in the literature. Fig. 3(a) shows the TiN [100] zone axis reciprocal lattice net, with the growth direction [001] and the non-specular direction [024] identified. Fig. 3(b) shows the Cu [ $\bar{1}12$ ] zone axis reciprocal lattice net, and that alignment of the Cu [ $\bar{1}12$ ] zone axis with the TiN [100] zone axis would put the Cu [110] direction in parallel with the growth direction and the non-specular Cu (402) reflection in the same scattering plane as the TiN

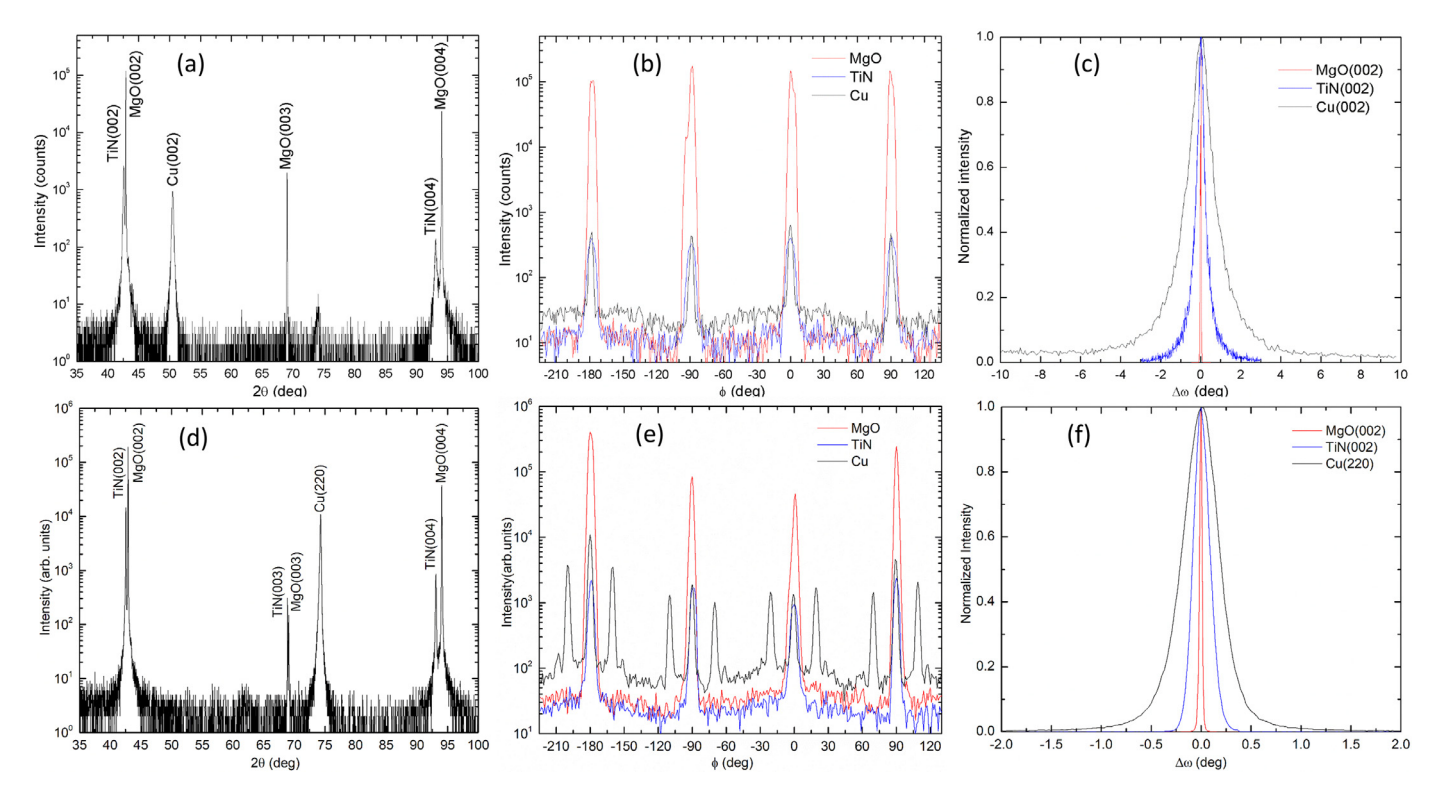


Fig. 2. XRD characterization of Cu/TiN bilayers: (a)  $\theta/2\theta$  scan, (b) 360°  $\phi$  scans on (024) reflections of MgO, TiN, and Cu, (c)  $\omega$  rocking curve scans on (002) reflections obtained from one specimen with Cu grown at 75 °C; (d)  $\theta/2\theta$  scan, (e) 360°  $\phi$  scans on (024) reflections of MgO and TiN and (402) reflection of Cu, (f)  $\omega$  rocking curve scans on (002) reflections of MgO/TiN and (220) reflection of Cu obtained from one specimen with Cu grown at 105 °C.

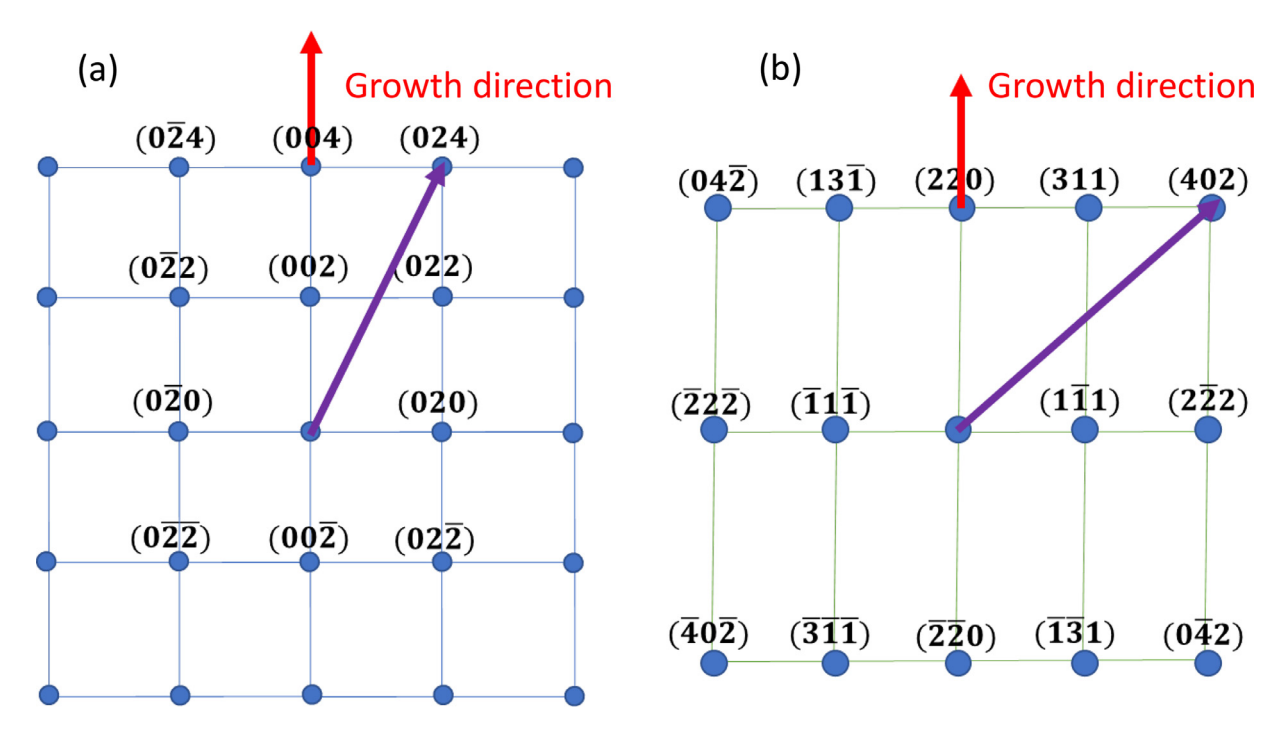


Fig. 3. Schematic reciprocal lattice points and directions for TiN and Cu: (a) the TiN [100] zone axis reciprocal lattice net; (b) the Cu[ $\bar{1}12$ ] zone axis reciprocal lattice net. Red and purple arrows in (a) and (b) denote respectively the growth direction and the directions of the off-specular XRD  $\phi$  scans shown in Fig. 2.

(024) reflection. This OR between the TiN buffer layer and the Cu top layer is Cu(110)//TiN(001) and Cu [ $\bar{1}12$ ]//TiN[100]. In Fig. 2(e), the existence of a group of three Cu (402) reflections peaks in the asymmetric 360°  $\phi$  scan, repeating at 90° intervals, can be understood by realizing that this Cu-TiN OR has different variants that are crystallo-

graphically equivalent. Fig. 4(a) and 4(b) show respectively schematics of the TiN (001) plane and the Cu (110) plane, together with various in-plane crystallographic directions. Fig. 4(c) shows the orientational relationship between TiN and Cu identified in Fig. 3, namely, Cu(110)//TiN(001), Cu  $[\bar{1}12]$ //TiN[100], and Cu  $[\bar{1}1\bar{1}]$ //TiN  $[0\bar{1}0]$  (vari-

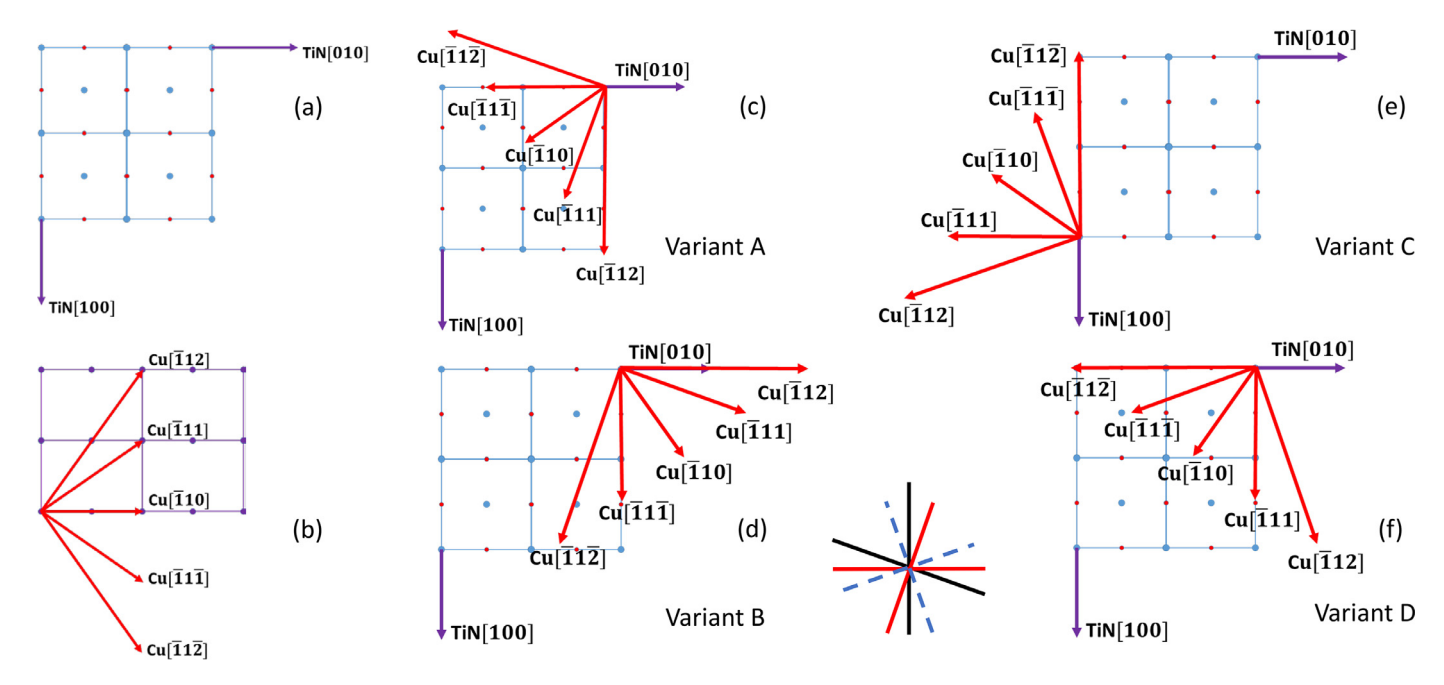


Fig. 4. Schematic real lattice points and directions for TiN and Cu: (a) the TiN (001) face with arrows indicating in-plane  $\langle 100 \rangle$  directions; (b) the Cu (110) face with arrows indicating various in-plane directions; (c)/(d)/(e)/(f) relationships between lattice directions within the TiN (001) plane and lattice directions within the Cu (110) plane. The orientational relationship variants A, B, C, and D, illustrated respectively in (c)/(d)/(e)/(f) are crystallographically equivalent. The inset shows that the in-plane Cu  $\langle 112 \rangle$  directions from the four variants form a triplet rotated with respect to each other by  $\pm 19.47^{\circ}$  and repeated at 90° intervals, consistent with data shown in Fig. 2(e) (black and red solid lines correspond to variants A and B, blue dashed lines correspond to additional  $\langle 112 \rangle$  directions arising from variants C and D).

ant A). Fig. 4(d) shows one variant crystallographically equivalent to that shown in Fig. 4(c): Cu(110)//TiN(001), Cu [112]//TiN[010] and Cu[111]//TiN[100] (variant B). It is noted that variants A and B are rotated 90° in-plane with respect to each other. Fig. 4(e) and 4(f) show respectively two other crystallographically equivalent variants: Cu(110)//TiN(001),  $Cu[\bar{1}1\bar{2}]//TiN[\bar{1}00]$  and  $Cu[\bar{1}11]//TiN[0\bar{1}0]$  (variant C); Cu(110)//TiN(001), Cu[112]//TiN[010] and Cu[111]//TiN[100] (variant D). The inset of Fig. 4 shows that the in-plane Cu <112> directions from the four variants form a triplet rotated with respect to each other by 19.47° (e.g., the angle between the vectors  $[\bar{1}11]$  and  $[\bar{1}12]$ ) and repeated at 90° intervals, in good agreement with the angles between the triplet peaks,  $\sim 19.6^{\circ}$ , observed in the asymmetric  $360^{\circ} \phi$  scans shown in Fig. 2(e). All four orientation variants, A, B, C, and D, can be summarized as Cu(110)//TiN(001) in the growth direction, Cu<111>//TiN<100> and Cu<112>//TiN<100> in the growth plane. This new OR between Cu and TiN is denoted as OR2. It is also noted that variants A and C are twin-related: forming an in-plane (111) twin with Cu<111>//TiN[010] in Fig. 4(c) and 4(e). Likewise, variants B and D are twin-related: forming an in-plane (111) twin with Cu<111>//TiN[100] in Fig. 4(d) and 4(f). These two groups of twins would be 90° rotated in-plane. The 90° in-plane rotated lenticular surface morphology shown in Fig. 1(c) is believed to be a manifestation of the fact that variants A and B are rotated 90° in-plane, as shown in Fig. 4(c) and 4(d).

Fig. 5 documents further changes in Cu/TiN bilayer specimens on MgO(001) substrates as the Cu growth temperature increases beyond 105 °C. Fig. 5(a) and 5(b) show  $\theta/2\theta$  scans from another two Cu/TiN/MgO(001) specimens with the Cu top layers growth temperatures of 180 °C and 250 °C, respectively. In contrast to data shown in Fig. 2, further rise in the Cu growth temperature led to the appearance of both Cu (002) and (220) reflections, indicating that the Cu top layers grown on TiN(001) templates at 180 °C and 250 °C are no longer perfectly textured, but polycrystalline with a mixed  $\langle 001 \rangle$  and  $\langle 110 \rangle$  texture in the growth direction. The XRD data shown in Fig. 5 are consistent with the polycrystalline contrast exhibited by the Cu layers shown in Fig. 1(f) and 1(h). XRD data shown in Figs. 2 and 5 document changes

in OR between the Cu top layer and the TiN(001) template as the Cu growth temperature changes: OR1 at 75  $^{\circ}\text{C};$  OR 2 at 105  $^{\circ}\text{C};$  and polycrystalline growth at 180  $^{\circ}\text{C}$  and 250  $^{\circ}\text{C}.$ 

Fig. 6(a), 6(b), and 6(c) show respectively XRD symmetric  $\theta/2\theta$  scans from Cu/TiN/MgO(001) specimens, with the Cu top layers grown at the same temperature of 105 °C to different thicknesses of 180 nm, 380 nm, and 1170 nm. Aside from (002) and (004) reflections of MgO and TiN, only the Cu (220) reflection is present. Fig. 6(d) shows the Cu (402) asymmetric  $360^{\circ} \phi$  scans corresponding to Fig. 6(a–c). The same group of triplet peaks are observed to repeat at 90° intervals, with an angular spacing between peaks at  $\sim 19.6^{\circ}$ . Data shown in Fig. 6(a-d) indicate that the presently observed new OR2 between Cu and TiN is robust and persists for Cu layers grown at 105 °C onto TiN(001) templates to wide ranging thicknesses. Fig. 6(e) shows the Cu (220)  $\omega$  rocking curve scans corresponding to Fig. 6(a-c). The rocking curve FWHM decreases with increasing Cu layer thickness, from 0.59° at 180 nm and 0.55° at 380 nm to 0.4° at 1170 nm. The mosaic spread of the Cu top layer, judged by the Cu (220)  $\omega$  rocking curve width, is smaller than that for the Cu top layer grown at 75 °C in the cube-on-cube orientation, as shown in Fig. 2.

Fig. 7 shows plan-view TEM characterization of the same Cu/TiN/MgO(001) specimen whose XRD symmetric  $\theta/2\theta$  scan is shown in Fig. 6(c). Plan-view TEM specimens were prepared by OmniProbe lift-out of a thin Cu/TiN slice without the MgO substrate by placing the Cu/TiN/MgO(001) specimen in the cross section orientation, followed by  $Ga^+$  ion beam thinning from the TiN side until all TiN is removed and a final Ar<sup>+</sup> ion polishing at 100 eV energy to electron transparency. The final TEM specimen consisted only of the Cu top layer. Fig. 7(a) shows a SAD pattern obtained with the zone axis placed approximately parallel to the growth direction, perpendicular to the thin specimen slice. As shown in Fig. 7(a), the SAD pattern consists of a superimposition of three Cu [110] zone axis diffraction patterns. The in-plane rotation angle between them is  $\sim \pm 19.5^{\circ}$ , consistent with the XRD results shown in Figs. 2 and 6. In addition, twinning spots with respect to in-plane (111) directions are observed, indicating the presence of twinning on {111} planes within the Cu top layer. Fig. 7(b) and 7(c) show a BF/DF im-

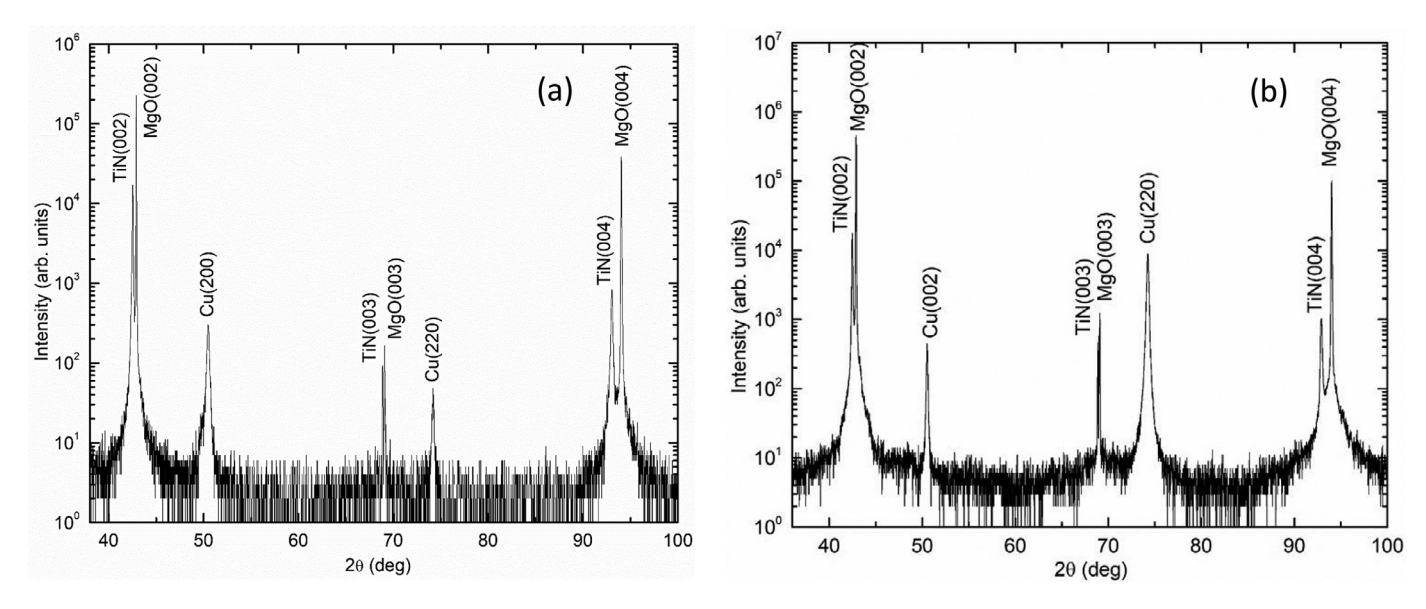


Fig. 5. XRD  $\theta/2\theta$  scans from Cu/TiN/MgO(001) specimens with the Cu layer deposited at (a) 180 °C; (b) 250 °C.

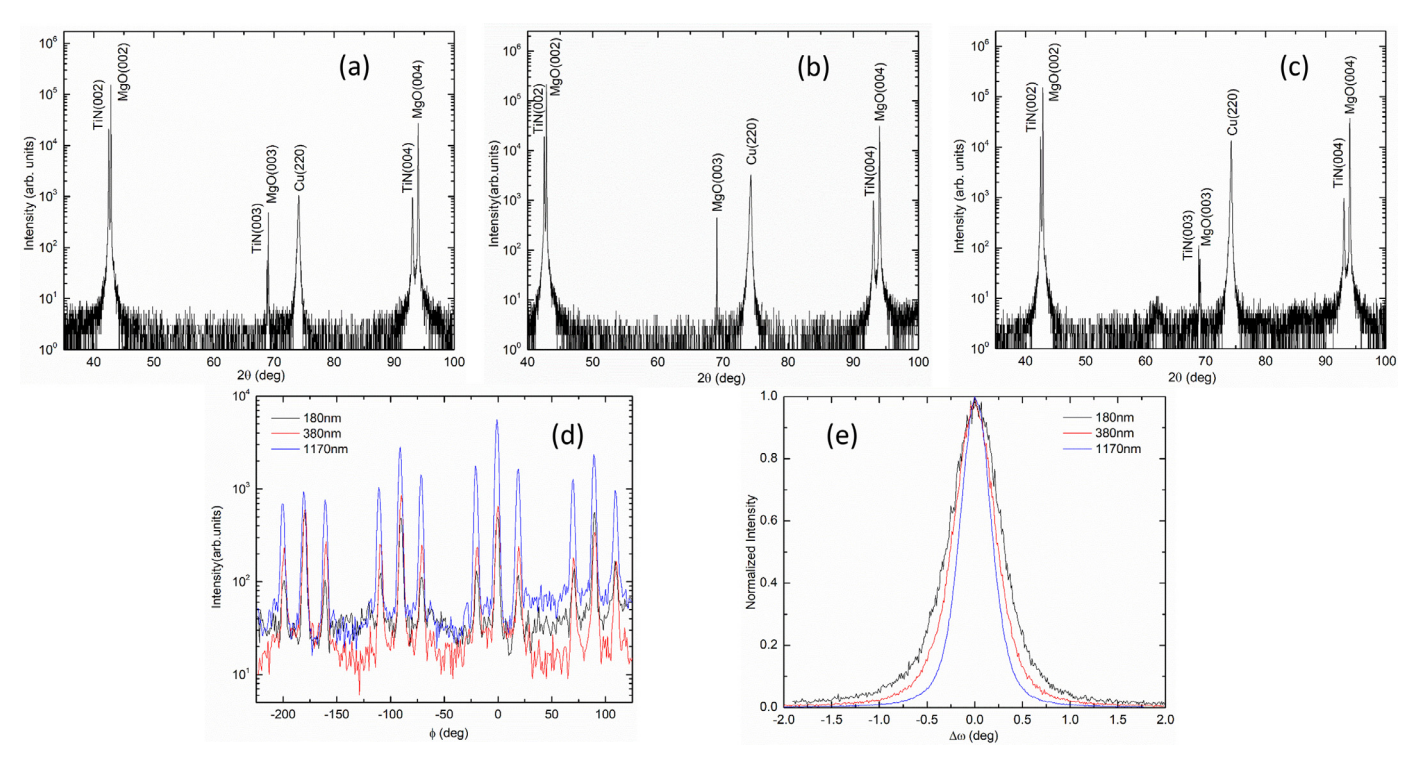


Fig. 6. XRD characterization of additional Cu/TiN/MgO(001) specimens with the Cu layer grown at 105 °C: (a)/(b)/(c)  $\theta/2\theta$  scans from specimens with increasing Cu layer thicknesses of 180 nm, 380 nm, and 1170 nm, keeping the TiN buffer layer thickness fixed at ~330 nm; (d) corresponding asymmetric 360°  $\phi$  scans on the (402) reflection of Cu; (e) corresponding  $\omega$  rocking curve scans on the Cu (220) reflection.

age pair of the Cu area from which the SAD in Fig. 7(a) was obtained. The BF/DF image pair delineates the portion of the Cu layer that belongs to one of the orientation variants illustrated in Fig. 4: apparently random shaped domains nestled together to form one continuous Cu layer. The DF image shown in Fig. 7(c) suggests that each domain goes through the entire thickness of the Cu layer. Within each domain, numerous nanoscale twin planes are seen to be present perpendicular to the in-plane  $\langle 111 \rangle$  direction. The BF image shown in Fig. 7(b) shows that the in-plane  $\langle 111 \rangle$  nanotwins exist in two mutually perpendicular directions, consistent with the crystallographic symmetry displayed in Fig. 4. While a preponderance of twins on  $\{111\}$  planes is often observed in va-

por phase deposited Cu thin films, the {111} twin plane normal is most often observed to be parallel to the growth direction [33]. The present case differs in having the {111} twinning plane normal perpendicular to the growth direction.

The out-of-plane d-spacing values measured from XRD symmetric  $\theta/2\theta$  scans shown in Fig. 2(a), 2(d), 5(a), and 5(b) are listed in Table 1. Measured d-spacing values for MgO and TiN show good agreement between specimens: with relative variations  $< 2 \times 10^{-4}$  and  $< 1.5 \times 10^{-3}$  for  $d_{004}(MgO)$  and  $d_{004}(TiN)$ , respectively. Fig. 8 shows results of X-ray reciprocal space mapping performed on the Cu/TiN/MgO(001) specimen with a Cu growth temperature of 75 °C and the Cu top layer

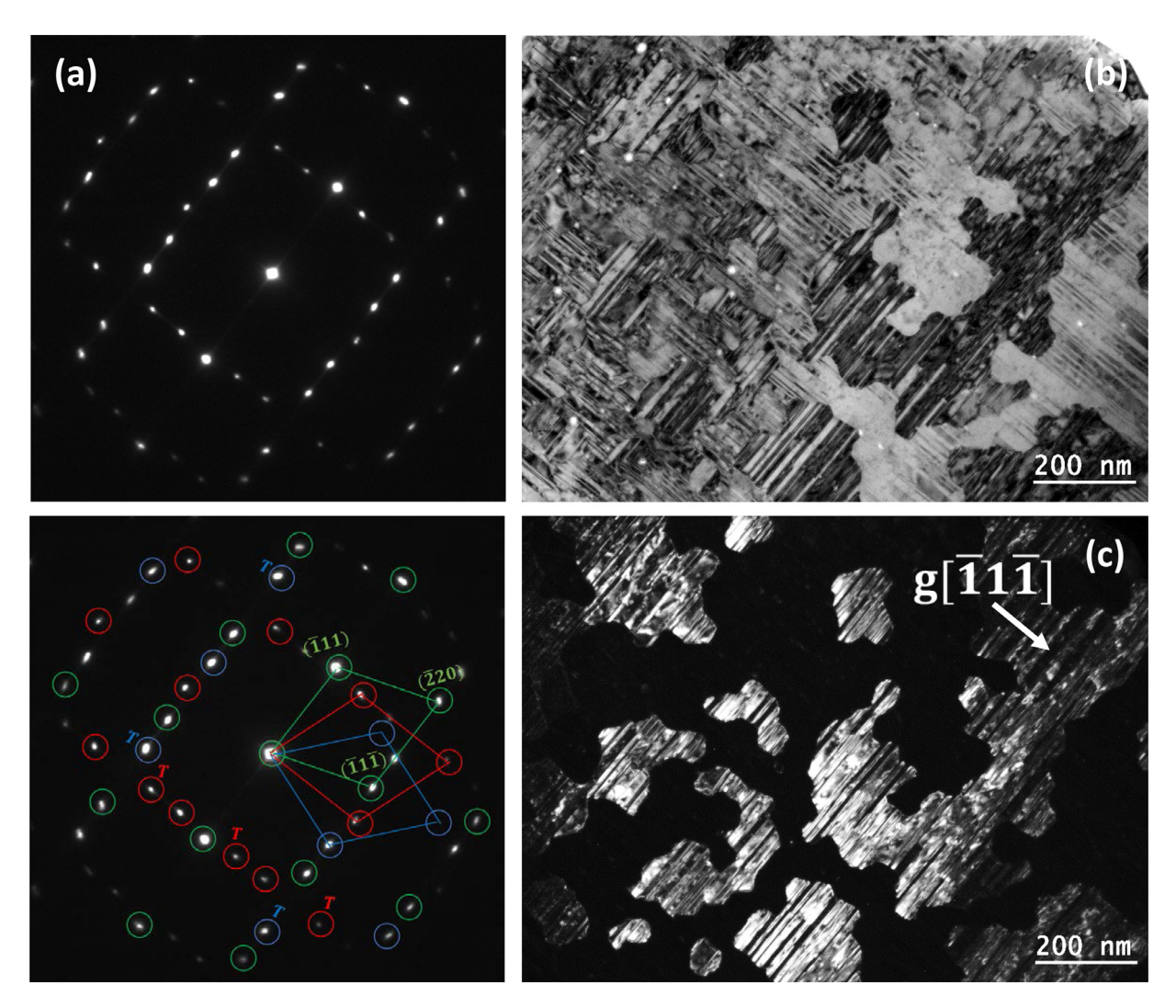


Fig. 7. TEM characterization of the Cu top layer of one Cu/TiN bilayer grown on MgO(001) with Cu(110)//TiN(001)//MgO(001): (a) a plan-view SAD from the Cu top layer with the zone axis aligned with the growth direction (top left panel), together with a superposition of three Cu [110] zone axis diffraction patterns consisting of red, green, and blue circles (bottom left panel). Red, green, and blue circles mark diffraction spots belonging to the same orientation variant. For clarity, (hkl) designations are only given for the green variant. The three variants are rotated in-plane with an angle of  $\sim \pm 19.5^{\circ}$ . The symbol T denotes  $\{111\}$  twinning spots; (b)/(c) a BF/DF image pair from the same area of the Cu top layer. The arrow in (c) denotes the direction of the  $[\bar{1}1\bar{1}]$  reciprocal vector of the red variant in (a).

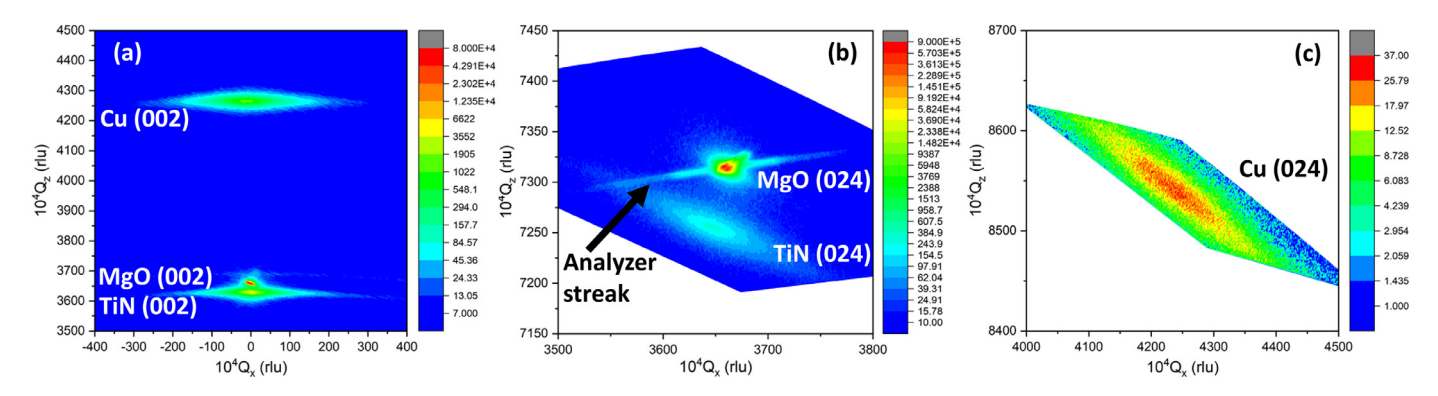


Fig. 8. X-ray RSMs of one Cu/TiN/MgO(001) specimen with a Cu growth temperature of 75 °C and the Cu top layer and TiN buffer layer in the cube-on-cube orientation: (a) RSM around (002) of MgO, TiN, and Cu; (b) RSM around (024) of MgO and TiN; (c) RSM around (024) of Cu. Reciprocal space coordinates are given in reciprocal lattice units (rlu),  $1 \text{ rlu} = 1.2982 \text{ Å}^{-1}$ .

**Table 1** Out-of-plane d-spacing values measured from XRD symmetric  $\theta/2\theta$  scans as a function of the Cu growth temperature, with raw data curves displayed in Figs. 2 and 5.

Cu growth	MgO d-s <sub>j</sub>	MgO d-spacing (Å)		TiN d-spacing (Å)		Cu d-spacing (Å)	
temperature ( °C)	(002)	(004)	(002)	(004)	(002)	(220)	
75	2.1064	1.0529	2.1229	1.0612	1.8061	n/a*	
105	2.1062	1.0529	2.1229	1.0612	n/a*	1.2757	
180	2.1062	1.0529	2.1235	1.0616	1.8064	1.2773	
250	2.1076	1.0531	2.1265	1.0628	1.8049	1.2764	

<sup>\*</sup> not observed.

and TiN(001) template in OR1, whose symmetric  $\theta/2\theta$  scan is shown in Fig. 2(a). Fig. 8(a) shows the RSM collected around (002) reflections of MgO, TiN, and Cu, with reciprocal space coordinates expressed relative to the reciprocal lattice unit (rlu), 1 rlu =  $2/\lambda = 1.2982 \text{ Å}^{-1}$ [34]. The in-plane and growth directions, [020] and [002] of MgO and TiN, are aligned respectively with the reciprocal space  $\hat{x}$  and  $\hat{z}$  directions shown in Fig. 8. Measured reciprocal space locations of MgO, TiN, and Cu (002) peaks, (Qx, Qz), are listed in Table 2. The RSM results show that MgO[002] and TiN[002] are aligned to within 0.07°, and that Cu[002] and TiN[002] are aligned to within 0.3°. The peak widths in the reciprocal space  $\hat{x}$  direction are consistent with  $\omega$  rocking curve data shown in Fig. 2(c). The (002) d-spacings obtained from the RSM data are 2.1051 Å, 2.1224 Å, and 1.8065 Å for MgO, TiN, and Cu, respectively, in good agreement with the  $\theta/2\theta$  scan results shown in Table 1. The out-ofplane lattice constants of MgO, TiN, and Cu for this specimen, obtained by averaging data from the  $\theta/2\theta$  scan and RSM shown in Figs. 2(a) and 8(a), are  $a_{out}(MgO) = 4.2115 \pm 0.0013 \text{ Å}$ ,  $a_{out}(TiN) = 4.2451 \pm 0.0006 \text{ Å}$ , and  $a_{out}(Cu) = 3.6126 \pm 0.0006$  Å, respectively. The relative difference between  $a_{out}(MgO)$  and the MgO bulk lattice constant of 4.21 Å is within  $4 \times 10^{-4}$ . Fig. 8(b) and 8(c) show two RSMs collected respectively around (024) reflections of MgO and TiN and (024) reflection of Cu. Measured reciprocal space locations of MgO (024), TiN (024), and Cu (024) peaks are again shown in Table 2. Comparing the peak locations of MgO (002) and (024) obtained from the RSM data,  $(Q_x^{002} - Q_y^{024})/Q_x^{024} =$ +0.0002 and  $(Q_x^{024} - 2Q_x^{024})/2Q_x^{024} = -0.0002$ , the cubicity of the MgO substrate is thus seen to be satisfied to  $2 \times 10^{-4}$ .

It is then noted that  $Q_x^{024}(TiN)/[2Q_x^{024}(TiN)] = 0.9949$ , deviating from cubicity by  $> 5 \times 10^{-3}$  and indicating that the out-of-plane lattice parameter is larger than the in-plane lattice parameter. Assuming that this deviation from cubicity is due entirely to the presence of an equal-biaxial in-plane stress, then the ratio of the out-of-plane and in-plane components of the reciprocal lattice vector is related to the in-plane strain  $\epsilon_{in}$  and out-of-plane strain  $\epsilon_{out}$ . As shown in Supplemental Materials Sections S3 and S4,  $Q_z^{024}(TiN)/[2Q_x^{024}(TiN)] =$  $(1 + \varepsilon_{in})/(1 + \varepsilon_{out})$ , and  $\varepsilon_{out}/\varepsilon_{in} = -2v/(1 - v)$  where v is the Poisson's ratio. With the known Poisson's ratio in the [001] direction of TiN,  $v_{001}^{TiN} = 0.159$  [35], the in-plane strain of TiN is obtained to be compressive,  $\varepsilon_{in} = -0.0037$ . Based on the measured reciprocal space locations of the MgO (024) and TiN (024) peaks, shown in Table 2, the relative difference in the in-plane lattice parameters of TiN and MgO is calculated:  $[d^{020}(TiN) - d^{020}(MgO)]/d^{020}(TiN) =$  $[Q_x^{024}(MgO) - Q_x^{024}(TiN)]/Q_x^{024}(MgO) = +0.0033$ , less than the bulk lattice misfit between the MgO and TiN,  $\delta = (a_{\rm TiN} - a_{\rm MgO})/a_{\rm MgO} = +0.007$ , by -0.0037. This measured in-plane lattice parameter difference between TiN and MgO is therefore consistent with the  $\varepsilon_{in}$  value calculated from assuming an equal-biaxial in-plane stress/strain state for the TiN buffer layer. As  $a_{TiN}$  exceeds  $a_{MgO}$ , the pseudomorphic forces during TiN growth onto the MgO substrate tend to decrease the in-plane lattice constant of TiN absent full relaxation, leading to a non-zero in-plane compressive strain in the TiN buffer layer.

TiN is a refractory ceramic with a melting/decomposition temperature  $> 2900\,$  °C [7]. Once grown, subsequent structural relaxation

within the TiN layer at temperatures ( 300 °C is unlikely. As far as Cu growth is concerned, the TiN buffer layer can be considered as a growth template with a fixed lattice parameter. The RSM data displayed in Fig. 8 and tabulated in Table 2 show that  $Q_z^{024}(Cu)/[2Q_x^{024}(Cu)] = 1.0074$ , deviating from cubicity by  $\rangle$  7  $\times$  10<sup>-3</sup> and indicating that the outof-plane lattice parameter is smaller than the in-plane lattice parameter. Again assuming that this deviation from cubicity is due entirely to the presence of an equal-biaxial in-plane stress in the Cu layer, then  $Q_z^{024}(Cu)/[2Q_x^{024}(Cu)] = (1+\varepsilon_{in})/(1+\varepsilon_{out})$ . As shown in Supplemental Materials Section S5, the Poisson's ratio in the [001] direction of Cu is also known,  $v_{001}^{Cu}=0.419$ , and thus  $\epsilon_{out}/\epsilon_{in}=(-1)[2v/(1-v)]=-1.4423$ for Cu. The Cu in-plane strain is then obtained to be tensile,  $\varepsilon_{in} = +0.003$ . Noting that the bulk lattice constant of Cu,  $a_{Cu}$ , is substantially less than  $a_{TiN}$ , it is reasonable to expect that the pseudomorphic forces during Cu growth onto the TiN template tend to increase the in-plane lattice constant of Cu, leading to a non-zero in-plane tensile strain. It is also noted that a matching of 7 Cu unit cells to 6 TiN unit cells significantly reduces the lattice mismatch,  $(7a_{\text{Cu}} - 6a_{\text{TiN}})/6a_{\text{TiN}} = -0.0067$ . An exact 7-to-6 Cu/TiN supercell matching would also tend to increase the Cu in-plane lattice constant, still leading to a tendency of an in-plane tensile strain for Cu absent full relaxation.

Fig. 9 shows results of X-ray reciprocal space mapping performed on the Cu/TiN/MgO(001) specimen with a Cu growth temperature of 105 °C and the Cu top layer and TiN(001) template in OR2, whose symmetric  $\theta/2\theta$  scan is shown in Fig. 2(d). Fig. 9(a) and 9(b) show respectively two RSMs collected along the film growth direction, around the (002) reflections of MgO and TiN and the (220) reflection of Cu. Fig. 9(c) shows the RSM collected around the (024) reflections of MgO and TiN, and Fig. 9(d) shows the RSM collected around the (402) reflection of Cu. Again, the MgO and TiN [010] direction and [001] direction align respectively with the reciprocal space  $\hat{x}$  and  $\hat{z}$  directions. Measured reciprocal space locations of MgO, TiN, and Cu peaks, (Qx, Qz), are again listed in Table 2. The MgO [002] and TiN [002] directions are aligned to within 0.15°. The Cu [220] and TiN [002] directions are aligned to within 0.21°. The peak widths in the reciprocal space  $\hat{x}$  direction are again consistent with  $\omega$  rocking curve information shown in Fig. 2(c). The d-spacings obtained from the RSMs are: 2.1060 Å and 2.1227 Å respectively for (002) of MgO and TiN, and 1.2763 Å for (220) of Cu, in good agreement with the  $\theta/2\theta$  scan results shown in Table 1. The out-ofplane lattice constants of MgO, TiN, and Cu for this specimen, obtained by averaging data from the  $\theta/2\theta$  scan and RSM shown in Fig. 2(d) and 9(a-b), are  $a_{out}(MgO) = 4.2120 \pm 0.0004 \text{ Å}$ ,  $a_{out}(TiN) = 4.2453 \pm 0.0005 \text{ Å}$ , and  $a_{out}(Cu) = 3.6091 \pm 0.0012$  Å, respectively. The relative difference between the measured lattice constant for MgO and the bulk value of 4.21 Å is within  $5 \times 10^{-4}$ . As shown in more detail in Supplemental Materials Section S6, from the reciprocal space locations of the (002) and (024) peaks of MgO and TiN, the cubicity of the MgO substrate is seen to be satisfied to within  $1 \times 10^{-3}$ . The in-plane strain of the TiN buffer layer is again compressive.

Fig. 9(d) shows the RSM collected around the (402) reflection of Cu, with the peak location within the reciprocal space listed in Table 2. The measurement shows that  $Q_z^{402}(Cu)/Q_z^{402}(Cu)=0.8105$ . Fig. 3(b) shows that the in-plane and out-of-plane components of this reciprocal lattice vector are respectively [220] and [2½2], i.e., [402] =  $\hat{z}Q_{220} + \hat{x}Q_{2\bar{z}2}$ . Thus,  $Q_z^{402}(Cu) = Q_{220} = 1/d_{220} = \sqrt{(2^2+2^2+0^2)}/a_{out}$ , and  $Q_x^{402}(Cu) = Q_{2\bar{z}2} = 1/d_{2\bar{z}2} = \sqrt{(2^2+(-2)^2+2^2)}/a_{in}$ , where  $a_{in}$  and  $a_{out}$  are respectively the in-plane and out-of-plane lattice constant of Cu. Therefore,  $\frac{a_{in}}{a_{out}} = [\frac{Q_x^{402}(Cu)}{Q_x^{402}(Cu)}] \frac{\sqrt{(2^2+(-2)^2+2^2)}}{\sqrt{(2^2+2^2+0)}} = 0.9926$ . This ratio deviates from cubicity by  $> 7 \times 10^{-3}$ , and indicates that the out-of-plane lattice parameter is larger than the in-plane lattice parameter. A quantitative estimate of the in-plane and out-of-plane strains is difficult in this case because, 1) the Poisson's ratio is not isotropic in the (110) plane, 2) multiple domains exist within the Cu top layer as evidenced by the TEM data shown in Fig. 7. Ignoring such complications, if in-plane

Table 2 Reciprocal space locations of MgO, TiN, and Cu reflections obtained from RSM results on Cu/TiN/MgO(001) specimens whose XRD symmetric  $\theta/2\theta$  scans are shown in Fig. 2. The reciprocal space coordinates are given in reciprocal lattice units,  $1 \text{ rlu} = 1.2982 \text{ Å}^{-1}$ .

Cu growth temperature (°C)	MgO $(Q_x, Q_z)$ (1	MgO $(Q_x, Q_z)$ (rlu)		$TiN(Q_x, Q_z)$ (rlu)		Cu $(Q_x, Q_z)$ (rlu)			
	(002)	(024)	(002)	(024)	(002)	(220)	(024)	(402)	
75	(-0.00023, 0.36592)	(0.36584, 0.73152)	(0.00019, 0.36293)	(0.36463, 0.72556)	(-0.00194, 0.42639)	n/a*	(0.42380, 0.85391)	n/a*	
105	(-0.00017, 0.36577)	(0.36551, 0.73175)	(0.00076, 0.36289)	(0.36573, 0.72503)	n/a*	(0.00344, 0.60354)	n/a*	(0.74010, 0.59983)	

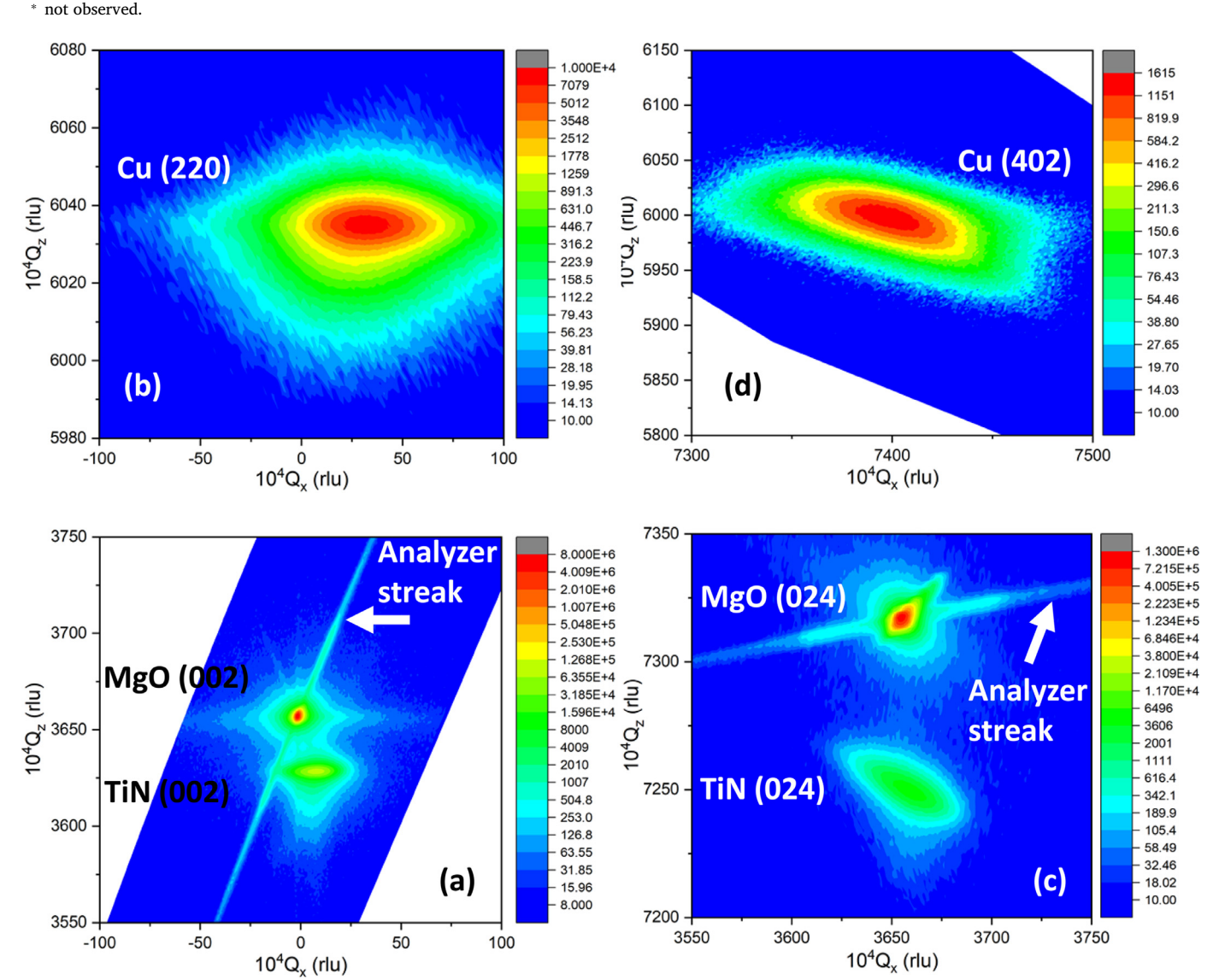


Fig. 9. X-ray RSMs of one Cu/TiN/MgO(001) specimen with a Cu growth temperature of 105 °C and Cu(110)//TiN(001)//MgO(001): (a) RSM around (002) of MgO and TiN; (b) RSM around (220) of Cu along the growth direction; (c) RSM around (024) of MgO and TiN; (d) RSM around (402) of Cu. Reciprocal space coordinates are given in reciprocal lattice units (rlu), 1 rlu = 1.2982  $\mathring{A}^{-1}$ .

isotropy and an equal-biaxial stress state are assumed, together with the assumption that the Poisson's ratio takes the value corresponding to polycrystalline Cu, v = 0.343, then  $0.9926 = (1 + \varepsilon_{in})/(1 + \varepsilon_{out})$  and  $\varepsilon_{out}/\varepsilon_{in} = (-1)[2v/(1-v)] = -1.0441$ . The Cu in-plane strain is thus estimated to be compressive,  $\varepsilon_{in} \approx -0.004$ . Data shown in Fig. 9(d) suggest the existence of an in-plane compressive strain within the (110) textured Cu top layer, although the actual strain magnitude is less certain due to complications described above.

The ORs between Cu and TiN and the associated natural dichromatic patterns (i.e., the bicrystal interfacial lattice pattern assuming the respective bulk lattice parameters [36]) at the Cu/TiN interfaces are illustrated in Fig. 10(a) and 10(b). The Cu/TiN OR1 is shown schematically in Fig. 10(a). In this case, lattices on both sides of the interface are square shaped, and a simple isotropic in-plane stretch is needed to bring Cu into coherency with TiN. The new Cu/TiN OR2 is shown schematically in Fig. 10(b). In this case, the lattice on the Cu side is a parallelogram, and an in-plane shear followed by an anisotropic in-plane normal straining is necessary to achieve Cu-TiN coherency. The presence of 90° rotated domains and twins at roughly equal volume fractions within each domain (Fig. 7(b-c)) leads to the triplet Cu (402) reflections shown in Fig. 2(e),

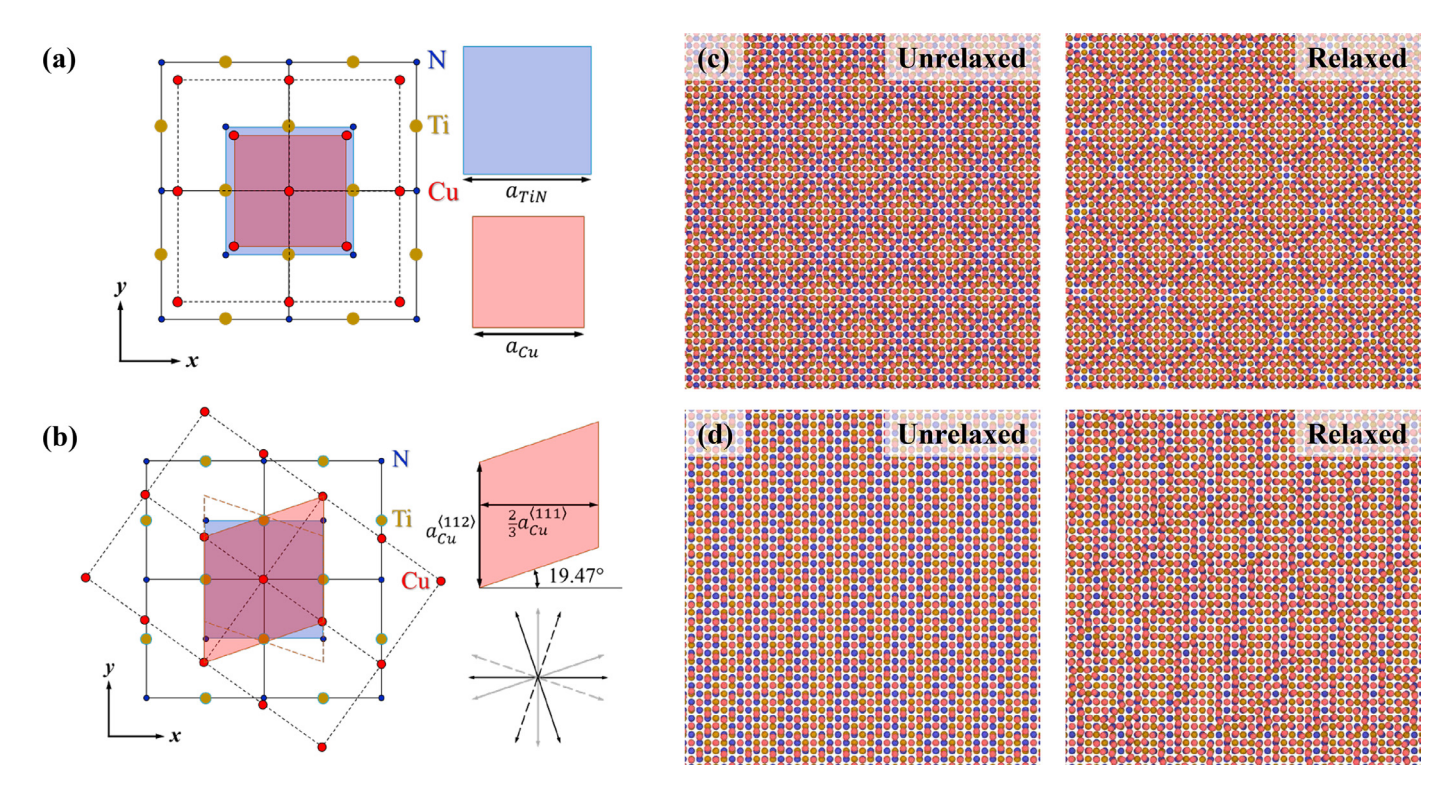


Fig. 10. Schematic illustrations of dichromatic patterns of the Cu/TiN interface: (a) OR1; (b) OR2; (c) atoms immediately adjacent to the interface for OR1, before (left) and after (right) MD relaxation; (d) atoms immediately adjacent to the interface for OR2, before (left) and after (right) MD relaxation. Atoms colored Red, Blue, and Orange represent Cu, N, and Ti, respectively. Solid and dashed lines in the inset correspond to (112) directions of the different OR variants.

again illustrated by the inset of Fig. 10(b) where the black and gray arrows with solid lines denote the in-plane  $\langle 112 \rangle$  directions arising from the two 90° rotated domains. The arrows with dashed lines denote new  $\langle 112 \rangle$  directions formed due to formation of twins.

As shown in Fig 10(c) and 10(d), after MD relaxation, Cu atoms show a strong affinity to N atoms and repulsion from Ti atoms, forming patches of small coherent regions. This is evident by observing that, after relaxation, the interfacial Cu atoms (red) shift towards N atoms (blue), but not Ti atoms (orange). It is interesting to note that the coherent regions in OR1 interfaces are squares, while those for OR2 interfaces are elongated parallelograms. Misfit dislocation networks formed, which separated the coherent regions.

Assuming the lattice constants parameterized in our MEAM potentials, i.e.,  $a_{\text{Cu}}=3.620$  Å and  $a_{\text{TiN}}=4.214$  Å, and neglecting the lattice strains in TiN, the in-plane lattice transformations in Cu (given by deformation gradient) necessary for OR1 and OR2 to achieve Cu-TiN coherency are respectively:

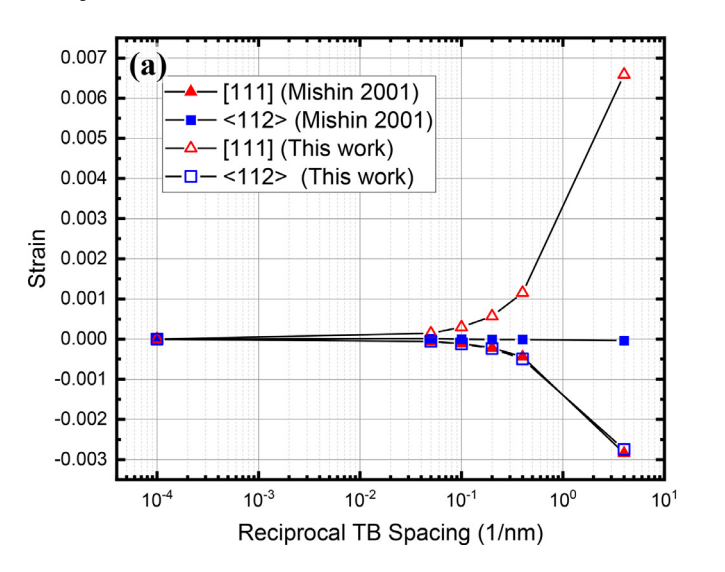
$$\begin{aligned} \mathbf{F}_1 &= \begin{bmatrix} 1.1641 & 0 \\ 0 & 1.1641 \end{bmatrix} \\ \mathbf{F}_2 &= \begin{bmatrix} 1.0082 & 0 \\ 0 & 0.9505 \end{bmatrix} \begin{bmatrix} 1 & 0 \\ -0.3536 & 1 \end{bmatrix} \end{aligned} \tag{1}$$

RSM data shown in Figs. 8 and 9 indicate that, for the interface with OR1, the Cu layer is under in-plane tension; while for the interface with OR2, the Cu layer is under in-plane compression. The in-plane tension experienced by the Cu layer in the OR1 interface is expected due to the presence of pseudomorphic forces, as seen in the expression of  $\mathbf{F}_1$  in Eq. (1). However, the applicability of this argument, when it comes to the OR2 interface, is less clear. As shown in Eq. (1), although  $\mathbf{F}_2$  contains a compression along one direction, it also has a tensile component in the other.

Given the high density of twin boundaries within the Cu layer revealed by TEM observations for the OR2 interfaces, Set 1 and Set 2  $\,$ 

simulations were conducted to assess the effect of twin boundary (TB) spacing on the equilibrium lattice constants in Cu at various temperatures. As shown in Fig. 11(a), at 0 K when Cu completely transforms to an HCP structure (this is equivalent to a TB spacing of ~2.5 Å), a significant lattice contraction ( $\sim$  -0.003 strain) is predicted by the Mishin EAM potential [30] perpendicular to the TBs ([111] direction), while no substantial changes occur in lattice spacings parallel to the TBs (along (112) directions). The temperature of 0 K was achieved via molecular statics by energy minimization using the conjugate gradient method. Although the magnitude of the maximum lattice contraction is comparable to what was observed in the experiment, it quickly decreases with the increase in TB spacing. When the TB spacing is 5-10 nm, as is shown in Fig. 7(b-c), the magnitude of lattice contraction in the [111] direction ranges from -0.00011 to -0.00022, one order of magnitude smaller than the experimental observations. Using the MEAM potentials developed in the present work, both lattice contraction and expansion are predicted. Interestingly, the present MEAM potentials predict a lattice contraction along the (112) direction, in contrast to the EAM prediction of lattice contraction of almost the same magnitude along [111]. A substantially larger lattice dilatation is predicted by the present MEAM potentials.

At finite temperatures, Fig. 11(b) shows that both the MEAM and the EAM potentials predicted linear thermal expansion perpendicular to the TBs larger than FCC Cu, and linear thermal expansion parallel to the TBs slightly smaller than FCC Cu. The EAM also predicted greater effects of TBs on these linear thermal expansion coefficients. The present MEAM potentials also predicted lightly higher overall thermal expansion coefficients than the EAM. This effect also diminishes quickly with increasing TB spacing: at a TB spacing of 5–10 nm, the deviation from bulk behavior is again small. To sum, for OR2, while the presence of TBs can contribute to the overall in-plane compression in Cu, this is likely not the sole or even the main contribution at the experimentally observed TB spacings.



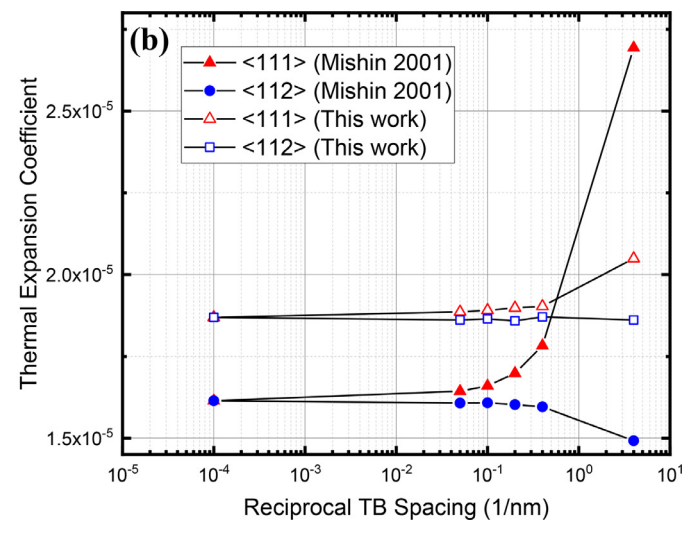
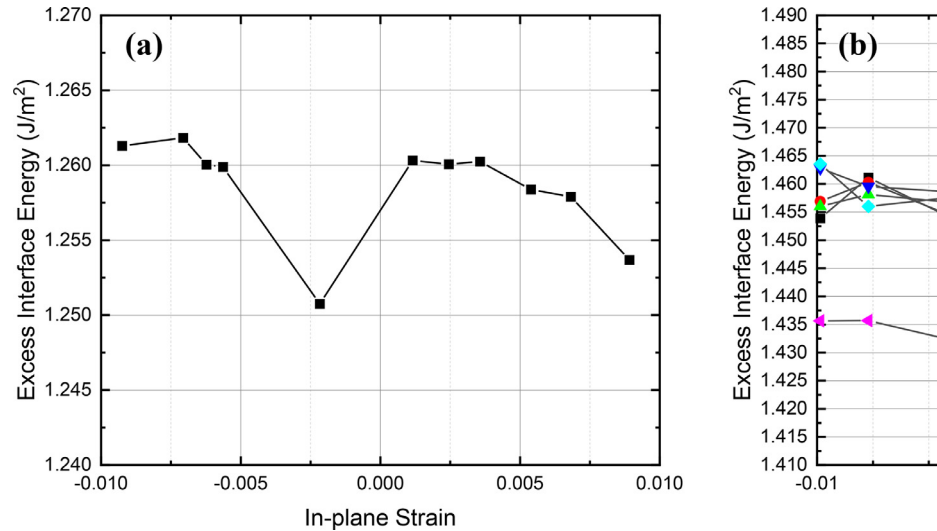


Fig. 11. Effects of twin boundary (TB) spacing on the equilibrium lattice constant of Cu at (a) 0 K; (b) effect of TB spacing on the linear thermal expansion coefficients. In (a), lattice constant changes are expressed as strains in the [111] direction (perpendicular to the TBs) and in the  $\langle 112 \rangle$  directions (parallel to the TBs). These strains are calculated based on a perfect FCC Cu lattice with a lattice constant of 3.62 Å for the potential developed in this work and 3.615 Å for the one developed by Mishin et al. [30]. The linear thermal expansion coefficients are calculated based on linear fits to changes in lattice spacings in the respective directions at 0–400 K. The TB spacing is given by its reciprocal. The pure FCC cases are represented by data points corresponding to a twin spacing of 10  $\mu$ m on the graphs.



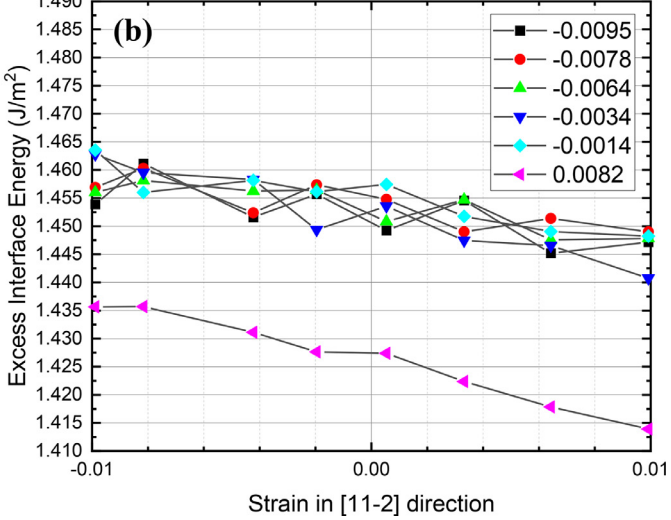


Fig. 12. Effect of in-plane stretch/compression of Cu on the excess interface energy of the Cu/TiN interface with (a) OR1; (b) OR2. The legend in (b) denotes the Cu layer strain in the [111] direction.

In-plane tension or compression of Cu with respect to TiN alters the interfacial coherency, the change in interfacial dislocation density may in turn impact the excess energy of the interface. To assess this, the Set 3 simulations aim to evaluate the effect of in-plane tension/compression of Cu layer on the interface energy, the result of which is shown in Fig. 12. In the OR1 case shown in Fig. 12(a), it is evident that in-plane isotropic straining of the Cu layer did not result in substantial changes in the interface excess energy, leading to only a variation of  $\sim 10 \text{ mJ/m}^2$  with no clear trend discernable. On the other hand, although the excess energy of the OR2 interface appears to decrease slightly with increasing Cu-layer tensile strains, the magnitude by which the excess energy changes is still not significant ( $\sim 50 \text{ mJ/m}^2$ ). The respective change in the interface excess energy for each OR appears especially insignificant when compared with the energy difference between the two ORs ( $\sim 200 \text{ mJ/m}^2$ ).

Fig. 13 displays the results of Set 4 simulations. Assuming the lattice constants parameterized in our MEAM potentials, i.e.,  $a_{\rm Cu}=3.620$  Å and  $a_{\rm TiN}=4.214$  Å, the excess energies of the OR1 and OR2 interfaces are

compared as a function of the MDN position. When the MDN is located at the chemical interface (corresponding to MDN position 0 shown in Fig. 13), the excess energy of the OR1 interface is lower than that of the OR2 by  $\sim 200 \text{ mJ/m}^2$ . Moving the MDN position into the Cu layer by 1, 2, 3, or 4 monolayers (corresponding to MDN position 1, 2, 3, and 4 shown in Fig. 13) appears to have little effect on the excess energy of the OR2 interface. However, the excess energy of the OR1 interface shows a more sensitive dependence on the MDN position, e.g., an energy fluctuation of  $\sim$ 400 mJ/m<sup>2</sup> occurs when the MDN position changes from 0 to 1. In other words, with one Cu atomic monolayer being fully coherent to the TiN template, the energetic relationship between the OR1 and OR2 interfaces would flip, resulting in the OR2 interface becoming energetically more favorable. As shown in Fig. 13, the energetic relationship between the OR1 and OR2 interfaces flips again as the MDN position changes from 1 to 2. The excess energy of the OR2 interface stays below that of OR1 at MDN positions of 3 and 4.

The MD simulations indicate that excess energies of the Cu/TiN interface in OR1 or OR2 are very close. According to the MD results shown

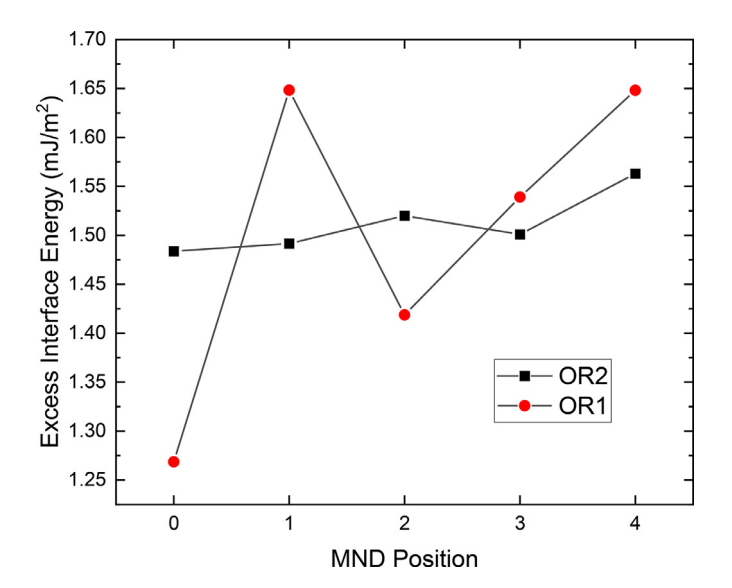


Fig. 13. Effect of position of the MDN inside Cu on the excess energy of the Cu/TiN interface with OR1 and OR2.

in Figs. 12 and 13, the maximum difference in interface excess energy between OR1 and OR2 is ~200 mJ/m<sup>2</sup>. In the crystal growth process, the first few Cu atomic monolayers could initially be coherent with the TiN substrate. During the deposition of subsequent layers, MDN is injected onto locations at or near the chemical interface. It is noted that the orientation of these coherent monolayers is unique (epitaxial to the TiN template). The later injection of MDN determines the orientation relationship between Cu and TiN. The selection of the orientation relation can be sensitive to the deposition temperature, as a difference of ~200 mJ/m<sup>2</sup> in the interface excess energy, when averaged to individual interfacial atoms, is comparable to their thermal energy at/near room temperature. As an estimate, assuming Cu adopting bulk density, two monolayers of Cu covering 1 m<sup>2</sup> amounts to  $\sim$ 4.4  $\times$  10<sup>19</sup> atoms. The maximum difference in interface excess energy between OR1 and OR2 would amount to ~29 meV per Cu atom, comparable to typical thermal energy at room temperature,  $\sim$ 26 meV (kT, where T = 300 K). MD results shown in Figs. 11 and 12 further indicate that the presence of nanoscale in-plane TBs and in-plane straining of the Cu layer do not change the energetic ranking of the OR1 and OR2 Cu/TiN interfaces in any significant way. As shown in Fig. 13, the energetic ranking of the OR1 and OR2 Cu/TiN interfaces is made even closer if the possibility of the MDN not being located at the chemical interface is considered. To sum, the MD simulation results suggest that interfacial energetics does not appear to be the dominant factor in determining whether the Cu/TiN interface adopts OR1 or OR2. This is consistent with the experimental observations shown in Fig. 2, that a mere change in growth temperature of 30 K would select one orientation relationship over another. It is surmised that this orientation selection at a slight change in growth temperature is more kinetic in nature.

The experimental observations shown in Fig. 5, namely another slight increase in growth temperature of 75 K, from 105 °C to 180 °C, would render the Cu layer polycrystalline with the Cu/TiN interface containing both OR1 and OR2 regions, are argued to be a further indication that kinetics, rather than energetics, is the dominant factor controlling low temperature Cu growth on TiN(001). Detailed kinetic mechanisms responsible for the presently observed orientation selection, non-existing at present to the best of our knowledge, as well as a tighter growth temperature bound for OR2 selection, remain to be elucidated through future work. The ability of controlling the Cu habit plane on TiN(001) templates by controlling the Cu growth temperature opens up the interesting possibility of testing the mechanical response

of Cu/TiN interfaces with Cu at different crystallographic orientations. Such work is also left for the future.

#### 4. Summary

We have conducted a series of Cu growth on TiN(001) templates via UHV magnetron sputter deposition. In addition to the previously reported Cu cube-on-cube growth on TiN(001) templates at close to room temperature, a new orientation relationship of Cu(110)//TiN(001) in the growth direction, Cu<111>//TiN<100> and Cu<112>//TiN<100> in-plane, was demonstrated for the first time, to the best of our knowledge, through raising the growth temperature by only 30 K. Raising the growth temperature further resulted in polycrystalline Cu growth, consistent with previous reports. Accompanying MD simulations using MEAM potentials newly developed for the Cu-TiN system computed interface energetics in both orientations, taking into account variations in the in-plane strain of the Cu layer and the presence of nanoscale twin boundaries within Cu. The MD results suggest that interfacial energetics is not the dominant factor in selecting the orientation relationship of the Cu/TiN interface, and points to future work investigating the role of kinetic pathways in selecting the actual orientation relationship between the Cu growth and the TiN template.

#### **Declaration of Competing Interest**

None.

#### Acknowledgements

The authors gratefully acknowledge partial project support from the NSF EPSCoR RII-Track 1 program, NSF OIA-1541079. Use of experimental resources at the LSU Shared Instrumentation Facility (SIF), a part of the NSF EPSCoR Consortium for Innovation in Manufacturing and Materials Core User Facilities (CIMM CUF), is acknowledged with thanks.

### Supplementary materials

Supplementary material associated with this article can be found, in the online version, at doi:10.1016/j.mtla.2020.100748.

#### References

- G. Yang, Y. Liu, Z. Hang, N. Xi, H. Fu, H. Chen, Adhesion at cerium doped metal-ceramic a-Fe/WC interface: a first-principles calculation, J. Rare Earths 37 (2019) 773–780.
- [2] F.Y. Lin, A. Chernatynskiy, J.C. Nino, J.L. Jones, R. Hennig, S.B. Sinnott, Role of composition and structure on the properties of metal/multifunctional ceramic interfaces, J. Appl. Phys. 120 (2016) 045310.
- [3] R. Polanco, A. De Pablos, P. Miranzo, M.I. Osendi, Metal–ceramic interfaces: joining silicon nitride–stainless steel, Appl. Surf. Sci. 238 (2004) 506–512.
- [4] S.B. Sinnott, E.C. Dickey, Ceramic/metal interface structures and their relationship to atomic- and meso-scale properties, Mater. Sci. Eng. R 43 (2003) 1–59.
- [5] S. Cazottes, Z.L. Zhang, R. Daniel, J.S. Chawla, D. Gall, G. Dehm, Structural characterization of a Cu/MgO(001) interface using Cs-corrected HRTEM, Thin. Solid Films 519 (2010) 1662–1667.
- [6] Z. Zhang, Y. Long, S. Cazottes, R. Daniel, C. Mitterer, G. Dehm, The peculiarity of the metal-ceramic interface, Sci. Rep. 5 (2015) 11460.
- [7] L.E. Toth, Transition Metal Carbides and Nitrides, Academic Press, New York and London, 1971.
- [8] B.W. Karr, I. Petrov, P. Desjardins, D.G. Cahill, J.E. Greene, In situ scanning tunneling microscopy studies of the evolution of surface morphology and microstructure in epitaxial TiN(001) grown by ultra-high-vacuum reactive magnetron sputtering, Surf. Coat. Technol. 94-95 (1997) 403-408.
- [9] S. Zhang, W. Zhu, TiN coating of tool steels: a review, J. Mater. Processing Technol. 39 (1993) 165–177.
- [10] L. Hultman, J.E. Sundgren, Structure/property relationships for hard coatings, in: R.F. Bunshah (Ed.), Handbook of Hard Coatings, Elsevier, Amsterdam, 2001.
- [11] C.A. Volkert, A.M. Minor, Focused ion beam microscopy and micromachining, MRS Bull. 32 (2007) 389–395.
- [12] Y. Mu, X. Zhang, J.W. Hutchinson, W.J. Meng, Measuring critical stress for shear failure of interfacial regions in coating/interlayer/substrate systems through a micro-pillar testing protocol, J. Mater. Res. 32 (2017) 1421–1431.

- [13] X. Zhang, B. Zhang, Y. Mu, S. Shao, C.D. Wick, B.R. Ramachandran, W.J. Meng, Mechanical failure of metal/ceramic interfacial regions under shear loading, Acta Mater. 138 (2017) 224–236.
- [14] X. Zhang, Y. Mu, M. Dodaran, S. Shao, D. Moldovan, W.J. Meng, Mechanical failure of CrN/Cu/CrN interfacial regions under tensile loading, Acta Mater. 160 (2018) 1–13.
- [15] X. Guo, Y. Zhang, Y.G. Jung, L. Li, J. Knapp, J. Zhang, Ideal tensile strength and shear strength of ZrO2(111)/Ni(111) ceramic-metal Interface: a first principle study, Mater. Des. 112 (2016) 254–262.
- [16] A. Sazgar, M.R. Movahhedy, M. Mahnama, S. Sohrabpour, A molecular dynamics study of bond strength and interface conditions in the Al/Al<sub>2</sub>O<sub>3</sub> metal–ceramic composites, Comput. Mater. Sci. 109 (2015) 200–208.
- [17] A.S.M. Miraz, S. Sun, S. Shao, W.J. Meng, B.R. Ramachandran, C.D. Wick, Computational study of metal/ceramic interfacial adhesion and barriers to shear displacement, Comput. Mater. Sci. 168 (2019) 104–115.
- [18] M. Vendruscolo, C.M. Dobson, Protein dynamics: Moore's law in molecular biology, Current Biol. 21 (2) (2011) R68–R70.
- [19] M. Dodaran, M.M. Khonsari, S. Shao, Critical operating stress of persistent slip bands in Cu, Comput. Mater. Sci. 165 (2019) 114–120.
- [20] W.C. Chen, C.Y. Peng, L. Chang, Heteroepitaxial growth of TiN film on MgO (100) by reactive magnetron sputtering, Nanoscale Res. Lett. 9 (2014) 551.
- [21] J.S. Chawla, X.Y. Zhang, D. Gall, Epitaxial TiN(001) wetting layer for growth of thin single crystal Cu(001), J. Appl. Phys. 110 (2011) 043714.
- [22] M.I. Baskes, R.A. Johnson, Modified embedded atom potentials for HCP metals, Model. Simul. Mater. Sci. Eng. 2 (1994) 147–163.
- [23] M.I. Baskes, J.S. Nelson, A.F. Wright, Semiempirical modified embedded-atom potentials for silicon and germanium, Phys. Rev. B 40 (1989) 6085–6100.
- [24] M.I. Baskes, Modified embedded-atom potentials for cubic materials and impurities, Phys. Rev. B 46 (1992) 2727–2742.

- [25] B.J. Lee, J.H. Shim, M.I. Baskes, Semiempirical atomic potentials for the fcc metals Cu, Ag, Au, Ni, Pd, Pt, Al, and Pb based on first and second nearest-neighbor modified embedded atom method, Phys. Rev. B 68 (2003) 144112.
- [26] B.J. Lee, M.I. Baskes, H. Kim, Y. Koo Cho, Second nearest-neighbor modified embedded atom method potentials for bcc transition metals, Phys. Rev. B 64 (2001) 184102.
- [27] B.J. Lee, M.I. Baskes, Second nearest-neighbor modified embedded-atom-method potential. Phys. Rev. B 62, 8564–8567 (2000).
- [28] S. Sun, B.R. Ramachandran, C.D. Wick, Solid, liquid, and interfacial properties of TiAl alloys: parameterization of a new modified embedded atom method model, J. Phys. Condens. Matter 30 (2018) 75002.
- [29] J. Hafner, Ab-initio simulations of materials using VASP: density-functional theory and beyond, J. Comput. Chem. 29 (2008) 2044–2078.
- [30] Y. Mishin, M.J. Mehl, D.A. Papaconstantopoulos, A.F. Voter, J.D. Kress, Structural stability and lattice defects in copper: ab initio, tight-binding, and embedded-atom calculations, Phys. Rev. B 63 (2001) 224106.
- [31] S. Plimpton, Fast parallel algorithms for short-range molecular dynamics, J. Comp. Phys. 117 (1995) 1–19.
- [32] A. Stukowski, Visualization and analysis of atomistic simulation data with OVITO the Open Visualization Tool, Model. Simul. Mater. Sci. Eng. 18 (2010) 015012.
- [33] A.M. Hodge, Y.M. Wang, T.W. Barbee, Mechanical deformation of high-purity sputter-deposited nano-twinned copper, Scripta Mater. 59 (2008) 163–166.
- [34] T. Konya, X-ray thin film measurement techniques III: high resolution X-ray diffractometry, The Rigaku J. 25 (2) (2009) 1–8.
- [35] W.J. Meng, G.L. Eesley, Growth and mechanical anisotropy of TIN thin films, Thin Solid Films 27 (1995) 108–116.
- [36] Y. Chen, S. Shao, X.-.Y. Liu, S.K. Yadav, N. Li, N. Mara, J. Wang, Misfit dislocation patterns of Mg-Nb interfaces, Acta Mater. 126 (2017) 552–563.

### Supplemental materials for

### Low temperature growth of Cu thin films on TiN(001) templates: Structure and Energetics

Xiaoman Zhang<sup>a</sup>, Shuai Shao<sup>b</sup>, A.S.M. Miraz<sup>c</sup>, C.D. Wick<sup>c</sup>, B.R. Ramachandran<sup>d</sup>, W.J. Meng<sup>a, i</sup>

<sup>a</sup>Department of Mechanical & Industrial Engineering, Louisiana State University Baton Rouge, Louisiana 70803, U.S.A.

<sup>b</sup>Department of Mechanical Engineering and the National Center for Additive Manufacturing Excellence, Auburn University, Auburn, Alabama 36849, U.S.A.

<sup>c</sup>College of Engineering & Science, Louisiana Tech University Ruston, Louisiana 71272, U.S.A.

<sup>d</sup>Institute for Micromanufacturing, Louisiana Tech University Ruston, Louisiana 71272, U.S.A.

# S1. Details on the parameterization of the modified embedded atom method (MEAM) potentials.

The modified embedded atom method (MEAM) that took second nearest neighbors into account was parameterized for this work [1, 2, 3, 4, 5, 6, 7, 8, 9, 10]. The parameters for N were taken from the literature [8], while new parameters were developed for Cu, Ti, and their mixtures (CuN, TiN, and CuTiN). The parameterization strategy is the same as our previous work utilizing a genetic algorithm fitting to a combination of experimental and density functional theory (DFT) properties for pure Cu, Ti, and their mixtures [11]. DFT calculations were performed in Vienna Ab-Initio Simulation Package (VASP) using the Perdew, Burke and Ernzerhof generalized gradient approximation for the exchange-correlation functional [12, 13, 14]. The Projector Augmented Wave pseudopotentials were used for core electrons [13, 14], and the valence electrons were expanded by a plane wave basis set with a cutoff energy of 400 eV. A 4×4×1 Γ-centered k-point mesh was used for all interfacial (surface energies and metal/ceramic systems), while a

\_

<sup>&</sup>lt;sup>i</sup> Corresponding author

4×4×4 mesh was used for all bulk calculations. The Monkhorst-Pack scheme was used for sampling the k-point of the plane wave basis in the first Brillouin zone [15].

The parameters arrived at for Ti and Cu are given in Table S1-1, and a comparison of different properties between new and existing MEAM models and DFT/experiment for Ti and Cu are given in Table S1-2. The minimum energy phase ( $E_0$ ) of Ti and Cu are hcp and fcc respectively. The other phases denoted with  $E_1$  and  $E_2$  are identified with the values given in the table for both the pure elements. All of these properties were included in the new model's parameterization. As is evident, generally good agreement is achieved by both the existing and the newly developed MEAM models. The generalized stacking fault energies (GSFEs) were also calculated for Ti and Cu as described in previous work [16]. From these, the minimum energy pathways can be identified and barriers to lateral displacement can be calculated. For displacement normal to the Ti (0001) surface, DFT, a model by Lee et al. [19] and our new model predict a barrier of 0.39, 0.29, and 0.39 eV, respectively. For displacements normal to Cu (001), DFT, a model by Baskes et. al. [17], and our new model give barriers of 0.75, 0.59, and 0.56 eV, respectively, while for Cu(111), they give barriers of 0.13, 0.23, and 0.14 eV, respectively. The new model is somewhat improved on GSFEs in comparison with existing models due to GSFEs being priorities in their parameterization.

The binary parameters arrived at for this work are given in Table S1-3. These were parameterized to reproduce experimental and DFT properties of TiN, CuTi, and CuN binary systems, along with some Cu/TiN interfacial properties. In addition to GSFE barriers, the work of adhesion (WoA) [34] between different metal/ceramic interfaces were calculated with DFT and the new models were parameterized to them. Table S1-4 gives a comparison of values between the new model and a model by Kim et al. [18] with DFT and experiment for different TiN, Ti2N, and Ti/TiN properties. Table S1-5 gives a comparison between the new model and a model by Kim et al. [35] with DFT and experiment for CuTi alloys. Finally, Table S1-6 gives a comparison between the new model with DFT and experiment for CuN (to our knowledge, no models for CuN have been developed). Additionally, the GSFE barriers for the Ti/TiN interface for DFT, the Kim model [18], and the new model are 1.78, 2.73, and 1.77 eV, respectively, showing good agreement for the new model.

Table S1-7 gives the ternary MEAM parameters arrived at for the current work. The WoA was compared between the new MEAM model and DFT for different interfaces. These include

the coherent Cu(001)/TiN(111) and a semi-coherent Cu(111)/TiN(111) interface as studied by DFT previously [34]. Table S1-8 gives a comparison between DFT and the new MEAM model for the WoA and GSFE barriers for these systems showing good agreement.

Table S1-1. Parameter sets for pure elements. Units of  $E_{\mathcal{C}}$  and  $r_{e}$  are in eV and Å respectively.

	$E_C$	$r_e$	α	Α	$\beta^{(0)}$	$eta^{(1)}$	$\beta^{(2)}$	$\beta^{(3)}$	$t_i^{(1)}$	$t_i^{(2)}$	$t_{i}^{(3)}$	$C_{min}$	$C_{max}$
Ti	4.87 <sup>a</sup>	2.92ª	4.75	1.09	3.16	1.38	1.53	0.0006	3.02	10.95	-8.88	0.80	2.80
Cu	3.54 <sup>b</sup>	3.61 <sup>b</sup>	5.12	1.07	3.96	3.38	7.16	0.68	4.34	2.14	3.17	0.8214	3.02

<sup>&</sup>lt;sup>a</sup>Ref. [18], <sup>b</sup>Ref. [17]

**Table S1-2.** Comparison of the DFT calculated or experimental properties of Cu and Ti with values obtained using existing models and the newly developed model in this work.

$\begin{array}{c ccccccccccccccccccccccccccccccccccc$	Properties		Ti			Cu	
$\begin{array}{c ccccccccccccccccccccccccccccccccccc$		Expt/DFT	Lee	New	Expt/DFT	Baskes	New
$\begin{array}{c ccccccccccccccccccccccccccccccccccc$				Model		[17]	Model
$\begin{array}{c ccccccccccccccccccccccccccccccccccc$	$E_{\text{vac}}\left(\text{eV}\right)$	1.27 <sup>a</sup> , 1.55 <sup>a</sup>	1.75	1.38	1.03 <sup>b</sup> , 1.19 <sup>c</sup>	1.12	1.11
$\begin{array}{c ccccccccccccccccccccccccccccccccccc$	$E_{\rm S}$ (001) (J/m <sup>2</sup> )		2.1416	1.65	$1.46^+, 1.44^f$	1.82	1.46
$ \begin{array}{c ccccccccccccccccccccccccccccccccccc$		1.92 <sup>e</sup>			1.44 <sup>g</sup>		
$ \begin{array}{c ccccccccccccccccccccccccccccccccccc$	Surface Energy				1 54+ 1 55g	1 74	1 43
$\begin{array}{c ccccccccccccccccccccccccccccccccccc$					1.54 , 1.55	1., .	11.15
$\begin{array}{c ccccccccccccccccccccccccccccccccccc$	Surface Energy				1.27+, 1.30f,	1.52	1.26
$\begin{array}{c ccccccccccccccccccccccccccccccccccc$	$(111) (J/m^2)$						
$\begin{array}{c ccccccccccccccccccccccccccccccccccc$	$E_1/E_0$	$0.957^{+}$	0.9956	0.9886	$0.9895^{+}$	1.0000	0.9898
$\begin{array}{c ccccccccccccccccccccccccccccccccccc$		$(E_1 \rightarrow bcc)$			$(E_1 \rightarrow bcc)$		
$\begin{array}{c ccccccccccccccccccccccccccccccccccc$	$E_2/E_0$	$0.982^{+}$	0.9906	0.9886	$0.9938^{+}$	0.9964	0.9962
$\begin{array}{c ccccccccccccccccccccccccccccccccccc$		$(E_2 \rightarrow fcc)$					
$\begin{array}{c ccccccccccccccccccccccccccccccccccc$							
$\begin{array}{c ccccccccccccccccccccccccccccccccccc$	$C_{11}$ (GPa)		170.04	156.27	$168.3^{1}$	172.49	151.40
$\begin{array}{c ccccccccccccccccccccccccccccccccccc$					1		
$\begin{array}{c ccccccccccccccccccccccccccccccccccc$	$C_{12}$ (GPa)		80.41	78.24	$122.1^{1}$	121.88	128.57
$\begin{array}{c ccccccccccccccccccccccccccccccccccc$	- C (CP)		74.70	00.20	<b>5.5.</b> 51	<b>5</b> 60 <b>5</b>	66.15
$\begin{array}{c ccccccccccccccccccccccccccccccccccc$	$C_{13}$ (GPa)		74.78	89.20	75.7	76.07	66.15
$\begin{array}{c ccccccccccccccccccccccccccccccccccc$			107.00	171 20			
$\begin{array}{c ccccccccccccccccccccccccccccccccccc$	C <sub>33</sub> (GPa)		187.09	1/1.30			
$\begin{array}{c ccccccccccccccccccccccccccccccccccc$	$C_{tt}(CD_0)$		12.09	40.00			
C <sub>66</sub> (GPa)       35.2 <sup>j</sup> , 44.81 39.01         Young Modulus       116.0 <sup>i</sup> 114.52 118.62       123.5 <sup>m</sup> 131.47 92.79         (GPa)       Shear Modulus       44.0 <sup>n</sup> 43.15 45.26       47.3 <sup>m</sup> 48.98 33.46         (GPa)	C44 (GFa)		42.08	49.99			
44.6k       Young Modulus     116.0i     114.52     118.62     123.5m     131.47     92.79       (GPa)     Shear Modulus     44.0n     43.15     45.26     47.3m     48.98     33.46       (GPa)	$C_{CC}(GP_2)$		11 81	30.01			
Young Modulus (GPa)       116.0i       114.52       118.62       123.5m       131.47       92.79         Shear Modulus (GPa)       44.0n       43.15       45.26       47.3m       48.98       33.46	C <sub>00</sub> (G1 a)		77.01	37.01			
(GPa) Shear Modulus 44.0° 43.15 45.26 47.3° 48.98 33.46 (GPa)	Young Modulus		114.52	118.62	123.5 <sup>m</sup>	131.47	92.79
Shear Modulus 44.0 <sup>n</sup> 43.15 45.26 47.3 <sup>m</sup> 48.98 33.46 (GPa)	C	110.0	11.102	110.02	123.0	151.17	,2.,,
(GPa)		44.0 <sup>n</sup>	43.15	45.26	47.3 <sup>m</sup>	48.98	33.46
D 11 M 1 1 100 7k 110 20 104 25 127 (m 120 77 120 10	(GPa)						
Bulk Modulus 109./* 110.29 104.25 13/.6" 138./5 136.18	Bulk Modulus	109.7 <sup>k</sup>	110.29	104.25	137.6 <sup>m</sup>	138.75	136.18
(GPa)	(GPa)						
Poisson Ratio 0.32-0.36 <sup>n, o*</sup> 0.33 0.31 0.34 <sup>m, p</sup> 0.34 0.38	Poisson Ratio	0.32-0.36 <sup>n, o*</sup>	0.33	0.31		0.34	0.38
$0.38^{q}$					$0.38^{q}$		

<sup>\*</sup> Average value for polycrystals

<sup>a</sup>Ref. [20], <sup>b</sup>Ref. [21], <sup>c</sup>Ref. [22], <sup>d</sup>Ref. [23], <sup>e</sup>Ref. [24], <sup>f</sup>Ref. [25], <sup>g</sup>Ref. [17], <sup>h</sup>Ref. [30], <sup>i</sup>Ref. [26], <sup>j</sup>Ref. [27], <sup>k</sup>Ref. [28], <sup>l</sup>Ref. [29], <sup>m</sup>Ref. [30], <sup>n</sup>Ref. [31], <sup>o</sup>Ref. [47], <sup>p</sup>Ref. [32], <sup>q</sup>Ref. [33]

<sup>&</sup>lt;sup>+</sup> DFT calculated in the present work

**Table S1-3.** Optimized parameters for binary systems. In any pair, the two elements are denoted by i and j respectively in C parameters such that  $C_{min}(\mathbf{Ti} - \mathbf{Ti} - \mathbf{N})$  is denoted by  $C_{min}(i - i - j)$  for TiN.

		(i-j) pair	
Parameters	TiN	CuTi	CuN
$E_C$	6.6563	4.2444	4.473
$r_e$	2.1073	2.7286	2.0609
α	4.7985	5.209	6.7074
$C_{min}(i-i-j)$	0.1884	0.8175	0.9292
$C_{min}(j-j-i)$	1.0379	0.8033	1.4
$C_{min}(i-j-i)$	1.404	0.7452	1.28155
$C_{min}(i-j-j)$	1.0771	1.2056	0.6442
$C_{max}(i-i-j)$	2.456	3.7663	1.6105
$C_{max}(j-j-i)$	1.8622	3.4894	1.4
$C_{max}(i-j-i)$	3.9865	3.1031	4.8395
$C_{max}(i-j-j)$	3.9645	1.7529	1.463
$\rho_0(j)/\rho_0(i)$	$18.00^{a}$	1.00	18.00

<sup>&</sup>lt;sup>a</sup> Ref. [18]

**Table S1-4.** Values of the properties reproduced by the new TiN binary model after fitting, compared with the experimental/DFT results and the values given by the Kim et al. [18] model.

Property	System		Expt/DFT	Kim et al.	This work
Lattica	TiN	а	4.241 <sup>a</sup>	4.242	4.214
Lattice constants (Å)	Ti <sub>2</sub> N	a c	$4.943^{a}$ $3.036^{a}$	4.7852 3.0465	5.0435 2.9011
		ι			
$\Delta_{ ext{mix}}H$	TiN		-1.74 <sup>b</sup>	-1.740	-1.781
(eV/atom)	Ti <sub>2</sub> N		-1.38 <sup>b</sup>	-1.633	-1.168
		<i>C</i> 11	625°	659.37	605.11
Elastic	TiN	$C_{12}$	165°	150.36	134.78
Constants		$C_{13}$	163°	183.39	103.08
(GPa)		<i>C</i> 33	$427^{d, e}, 440^{d, f}$	515.21	371.89
(Gra)		C44	179 <sup>d, e</sup> , 160 <sup>d, f</sup>	209.15	144.43
		C66	320°, 292 <sup>b</sup>	320.03	291.56
Surface		(001)	1.397*, 1.38 <sup>b, g</sup>	1.2717	1.3079
Energyies	TiN	(110)	2.523*, 2.59-2.86 <sup>b, h</sup>	2.4268	1.8395
$(J/m^2)$		(111)	$3.3230^*, 3.62^{b, g}$	3.6362	2.4377
WoA (J/m <sup>2</sup> )	Ti/TiN		7.01*	9.9	5.7

<sup>\*</sup>DFT calculated in the present work

<sup>&</sup>lt;sup>d</sup>Ref. [7], <sup>b</sup>Ref. [18], <sup>h</sup>Ref. [34, 35]

<sup>&</sup>lt;sup>a</sup>Ref. [36], <sup>c</sup>Ref. [37], <sup>f</sup>Ref. [38], <sup>g</sup>Ref. [39], <sup>e</sup>Ref. [40],

**Table S1-5.** Values of the properties reproduced by the new CuTi binary model after fitting, compared with the experimental/DFT results and the values given by the Kim et al. [35] model.

Property	System		Expt/DFT	Kim et al.	This work
	γ-CuTi	а с	3.107 <sup>a</sup> 5.919	3.132 6.257	3.17 6.03
_	CuTi <sub>2</sub>	а с	2.943 <sup>a</sup> 10.784	3.29 9.14	2.79 12.5
Lattice constants (Å)	Cu <sub>3</sub> Ti	а b с	5.162,° 5.45 <sup>b</sup> 4.347,° 4.307 <sup>b</sup> 4.531,° 4.426 <sup>b</sup>	5.96 4.33 4.47	5.40 4.31 4.89
	β-Cu <sub>4</sub> Ti	а b с	4.522 <sup>b</sup> 4.344 12.897	4.75 4.11 14.45	4.83 4.33 13.23
$\Delta_{\text{mix}}H$ (eV/atom)	γ-CuTi CuTi <sub>2</sub> Cu <sub>3</sub> Ti		-0.115, <sup>d</sup> -0.151* -0.091, <sup>e</sup> -0.143* -0.100*	-0.112 -0.067 -0.042	-1.40 -0.129 -0.123
Elastic Constants (GPa)	β-Cu <sub>4</sub> Ti γ-CuTi	C <sub>11</sub> C <sub>12</sub> C <sub>13</sub> C <sub>33</sub> C <sub>44</sub> C <sub>66</sub>	-0.090*  176.16* 93.64* 112.13* 175.59* 59.73* 66.37*	-0.055 196.46 60.32 101.82 213.30 91.81 115.38	-0.079 162.76 102.95 108.71 187.43 50.87 48.36
Surface Energies (J/m²)	γ-CuTi	(001) (110) (111)	2.51* 1.79* 2.05*	1.81 1.48 1.69	1.58 1.00 0.84

<sup>\*</sup>DFT-calculated in the present work

<sup>&</sup>lt;sup>a</sup>Ref. [41], <sup>b</sup>Ref. [42], <sup>c</sup>Ref. [43], <sup>d</sup>Ref. [44], <sup>e</sup>Ref. [45]

**Table S1-6.** Comparison between the properties reproduced by the new model in this work and the experimental/DFT target values.

Property	System		Expt/DFT	This work
Lattice constants (Å)	Cu <sub>3</sub> N	а	3.819 <sup>a</sup>	3.85
Lattice constants (Å)	CuN	a	4.1479*	4.1245
A II (aV/atam)	Cu <sub>3</sub> N		-3.646*	-3.732
$\Delta_{mix}H$ (eV/atom)	CuN		-4.529*	-4.476
	Cu <sub>3</sub> N	(001)	1.13*	1.13
Surface Energy, $E_{\rm S}$ (J/m <sup>2</sup> )	CuN	(001)	0.952*	1.03
	Cun	(111)	$0.945^{*}$	0.71

<sup>\*</sup>DFT-calculated in the present work

**Table S1-7.** Ternary parameters for CuTiN.

Parameters	Value
$C_{min}(Cu - N - Ti)$	0.5830
$C_{min}(Cu - Ti - N)$	1.0160
$C_{min}(Ti - N - Cu)$	0.7142
$C_{max}(Cu - N - Ti)$	2.4420
$C_{max}(Cu - Ti - N)$	2.3354
$C_{max}(Ti - N - Cu)$	1.4614

**Table S1-8.** Comparison of WoA and GSFE barrier heights calculated with DFT and our MEAM model for Cu/TiN interfacial systems.

	Wo	$A (J/m^2)$	GSFE barrier (J/m <sup>2</sup> )		
System	DFT	MEAM	DFT	MEAM	
Coherent Cu(001)/TiN(111)	1.90	1.73	1.03	1.02	
Semi-coherent Cu(111)/TiN(111)	3.17	2.52	0.06	0.06	

<sup>&</sup>lt;sup>a</sup>Ref. [46], [47]

# S2. Details on molecular dynamics (MD) simulations performed with the newly developed modified embedded atom method (MEAM) potentials

Using the MEAM potentials developed for the Cu-TiN system by the present authors, as documented in Section S1, as well as the Cu EAM potential developed by Mishin et al. [48], four sets of MD simulations were performed:

- (1) Set 1: to assess the effect of nano-twin boundary spacing on the equilibrium lattice constant of Cu;
- (2) Set 2: to assess the effect of nano-twin boundary spacing on the linear thermal expansion of Cu;
- (3) Set 3: to assess the effect of in-plane strains experience by the Cu layer on excess energies of Cu/TiN interfaces;
- (4) Set 4: to assess the effect of the location of misfit dislocation network (MDN) on the excess energy of the Cu/TiN interface.

Set 1 was conducted on a series of small Cu structures containing a few tens to hundreds of Cu atoms as shown in Fig. S2-1(a), with x- and z- axes aligned with  $[11\overline{2}]$  and  $[1\overline{1}0]$  directions, and the y- axis aligned with the [111] direction. These structures are fully periodic, each contains two evenly spaced twin boundaries, and differ in size only in the y- direction. Iterative search of the true ground state of each structure was performed by adjusting the strain in each direction followed by energy minimization using a conjugate gradient method.

Set 2 was conducted on the same set of small Cu structures in their ground states. To calculate the thermal expansion coefficient, each structure is equilibrated at finite temperatures of 100K~400K at zero pressure for 0.25 ns after a brief temperature ramp up of 0.03 ns. The ensemble used here is NPT, the timestep used is 0.002. The average dimensions in x, y, and z directions during the 0.25 ns equilibration period are calculated to reflect the thermally expanded Cu nanotwinned structures.

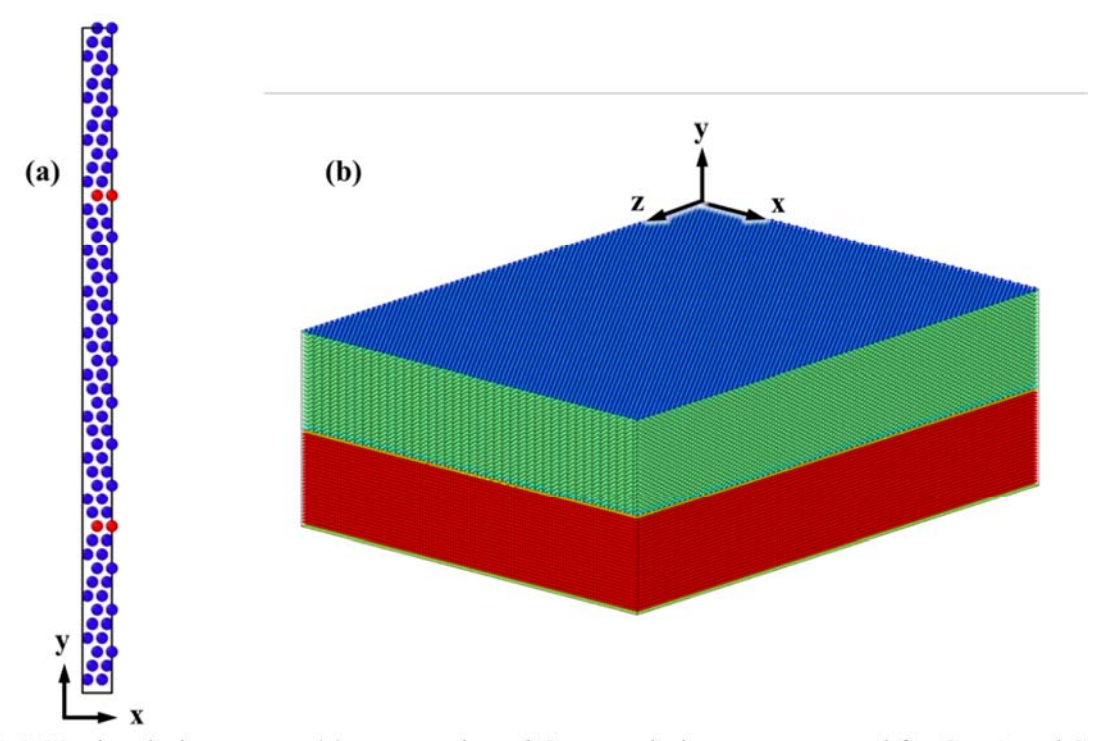


**Fig. S2-1**. MD simulation setup: (a) nano-twinned Cu atomistic structure used for Set 1 and Set 2 simulations; (b) Cu/TiN interface atomistic structure used for Set 3 and Set 4 simulations.

Set 3 simulations considered Cu/TiN interfaces with two different orientation relations (ORs). As described in detail in the main text, OR1 is the cube-on-cube orientation with Cu(001)//TiN(001) in the growth direction, while OR2 is Cu(110)//TiN(001) in the growth direction and Cu<111>//TiN<100> in-plane. For each OR, bicrystal structures were constructed, shown in Fig. S2-1(b), such that the interface is within the x-z plane while the misfit dislocation network (MDN) forms at the chemical interface. Periodic boundary conditions were applied to x and z directions, while the fixed boundary condition was applied in y. This boundary condition set has been commonly utilized for interfacial property calculations [49, 50, 51]. It was assumed that the TiN is stress free, while the Cu layer is subjected to in-plane stresses. The y- dimension of the structures was kept constant, while the x- and z- dimensions were varied so that the in-plane strains in the Cu layer can be adjusted. For instance, using the lattice constants parameterized in our MEAM potentials, i.e.,  $a_{\text{Cu}} = 3.620 \text{ Å}$ ,  $a_{\text{TiN}} = 4.214 \text{ Å}$ , 47 periodic lengths of Cu and 40 periodic lengths of TiN correspond to an in-plane strain of -0.0093 in Cu, while 15 periodic lengths of Cu and 13 periodic length of TiN corresponds to an in-plane strain of 0.0089 in Cu. In-plane strains

from  $\sim +1\%$  to  $\sim -1\%$  have been considered for both ORs. Since the interfaces with OR1 is four-fold symmetric, isotropic in-plane strains were applied. Anisotropic in-plane strains were applied for the interfaces with OR2. The energy of each structure was minimized using molecular statics while maintaining zero stress in the y- direction for each crystals. Interfacial excess energies were calculated using the formula:  $\gamma_{excess} = \frac{1}{A}(E_{inter} - ne_{Cu} - me_{Ti} - le_N)$ , where A is the area of the interface,  $E_{inter}$  is the total energy of the system containing one Cu/TiN interface, n, m, l and  $e_{Cu}$ ,  $e_{Ti}$ ,  $e_{N}$  are the number and reference energy of Cu, Ti, and N atoms, respectively.

Set 4 considered two series of bimetallic structures corresponding to each of the ORs. Each series varied the location of the MDN from the chemical interface to 4 atomic monolayers into Cu, away from the chemical interface. The location of the MDN was varied by introducing Cu atomic monolayers completely coherent to TiN so that the discontinuity in the in-plane lattice spacing happens away from the chemical interface. The boundary conditions utilized in these simulations were identical to the ones applied in Set 3. As will be detailed in the main text, results from Set 3 simulations showed that minor (± 1%) in-plane biaxial stretch and compression does not lead to significant change in the excess interface energy (40 mJ/m² at most, much smaller as compared to changes induced by the changes in MDN location, ~400 mJ/m²). For this reason, during minimization, only the y- stress components in both layers and all normal stress components in the TiN layer were maintained at zero. The Cu layers contained in-plane finite strains of 0.1~0.2%. The molecular dynamics/statics simulations were performed using the Large-scale Atomic/Molecular Massively Parallel Simulator (LAMMPS) [52]. The atomistic structures were visualized by the Open Visualization Tool [53].

# S3. Relating deviation of cubicity from X-ray reciprocal space mapping (RSM) measurements to in-plane and out-of-plane strains in cubic crystalline films

It is stated in the main text that the ratio of the out-of-plane and in-plane components of the reciprocal lattice vector is related to the in-plane strain  $\varepsilon_{in}$  and out-of-plane strain  $\varepsilon_{out}$ . For an ideal cubic structure with no deviation from cubicity, in-plane and out-of-plane lattice constants,  $a_{out}$  and  $a_{in}$ , are equal, as are in-plane and out-of-plane d-spacings,  $d_{in}^{hkl}$  and  $d_{out}^{hkl}$ . The Laue condition states that diffraction occurs when the scattering vector,  $\Delta \vec{k} = \vec{k} - \vec{k}_0$ , is equal to a reciprocal lattice vector  $\overline{Q^{hkl}}$ , with  $Q^{hkl} = 1/d^{hkl}$ . Here  $\vec{k}_0$  and  $\vec{k}$  are respectively the incident and scattered wave vector, and  $d^{hkl}$  is the d-spacing for the (hkl) plane [54].

Take as an example the case described in the main text, an off-specular diffraction peak,  $\overline{Q^{024}} = (Qx, Qz) = (0.36463, 0.72556)$  (see Table 2 in the main text), was observed for the TiN buffer layer in one Cu/TiN/MgO specimen with the Cu top layer grown at 75 °C and the Cu top layer and the TiN buffer layer in the cube-on-cube orientation. The out-of-plane and in-plane directions are  $\hat{z} = \text{TiN} [001]$  and  $\hat{x} = \text{TiN} [010]$ , respectively. The diffraction peak location was given in reciprocal lattice units (rlu), 1 rlu = 1.2982 Å<sup>-1</sup>. Noting that 1)  $\overline{Q^{024}} = \hat{z}Q_z^{024} + \hat{x}Q_x^{024}$ , 2)  $Q_z^{024} = Q^{004} = 0.72556$ ,  $Q_x^{024} = Q^{020} = 0.36463$ , 3)  $Q^{004} = 1/d^{004}$ , 4)  $2Q^{020} = Q^{040} = 1/d^{040}$ , we have

$$\frac{Q_z^{024}}{[20_x^{024}]} = \frac{0.72556}{2 \times 0.36463} = 0.9949 = \frac{d^{040}}{d^{004}}$$

$$=\frac{[(d^{040}-d^{040}_{ideal})+d^{040}_{ideal}]}{[(d^{004}-d^{004}_{ideal})+d^{004}_{ideal}]}=\left(\frac{d^{040}_{ideal}}{d^{004}_{ideal}}\right)\frac{\frac{(d^{040}-d^{040}_{ideal})}{d^{040}_{ideal}}}{\frac{(d^{004}-d^{004}_{ideal})}{d^{004}_{ideal}}}$$

$$=\frac{(1+\varepsilon_{in})}{(1+\varepsilon_{out})}$$

in which  $d_{ideal}^{040}=d_{ideal}^{004}$  are the in-plane and out-of-plane  $\{004\}$  d-spacing for the ideal lattice,  $\varepsilon_{in}=(d^{040}-d_{ideal}^{040})/d_{ideal}^{040}$ , and  $\varepsilon_{out}=(d^{004}-d_{ideal}^{004})/d_{ideal}^{004}$ .

# S4. Relating the ratio of out-of-plane and in-plane strains in an isotropic thin layer in an equal-biaxial stress state

For an isotropic thin layer in a Cartesian coordinate system  $\hat{1} - \hat{2} - \hat{3}$ , with in-plane directions  $\hat{1}$  and  $\hat{2}$ , and out-of-plane direction  $\hat{3}$ , an equal-biaxial in-plane stress state is characterized by the stress matrix  $\sigma$ ,

$$\boldsymbol{\sigma} = \begin{pmatrix} \sigma_1 \\ \sigma_2 \\ \sigma_3 \\ \sigma_4 \\ \sigma_5 \\ \sigma_6 \end{pmatrix} = \begin{pmatrix} \sigma \\ \sigma \\ 0 \\ 0 \\ 0 \\ 0 \end{pmatrix},$$

in which  $\sigma_1 = \sigma_2 = \sigma$  are the in-plane stresses, the out-of-plane stress  $\sigma_3$  and the shear stresses  $\sigma_4$ ,  $\sigma_5$ , and  $\sigma_6$  are zero. Noting that the elastic compliance matrix S is

$$S = \begin{pmatrix} \frac{1}{E} & \frac{-v}{E} & \frac{-v}{E} & 0 & 0 & 0 \\ \frac{-v}{E} & \frac{1}{E} & \frac{-v}{E} & 0 & 0 & 0 \\ \frac{-v}{E} & \frac{-v}{E} & \frac{1}{E} & 0 & 0 & 0 \\ \frac{-v}{E} & \frac{-v}{E} & \frac{1}{E} & 0 & 0 & 0 \\ 0 & 0 & 0 & \frac{2(1+v)}{E} & 0 & 0 \\ 0 & 0 & 0 & 0 & \frac{2(1+v)}{E} \end{pmatrix},$$

in which E and  $\nu$  are respectively the Young's modulus and the Poisson's ratio, and that the strain matrix  $\epsilon = S\sigma$ , with

$$\boldsymbol{\varepsilon} = \begin{pmatrix} \epsilon_1 \\ \epsilon_2 \\ \epsilon_3 \\ \epsilon_4 \\ \epsilon_5 \\ \epsilon_6 \end{pmatrix},$$

we have for the in-plane strain,  $\epsilon_{in} = \epsilon_1 = \epsilon_2 = [(1-v)/E]\sigma$ , and the out-of-plane strain,  $\epsilon_{out} = \epsilon_3 = [(-2v)/E]\sigma$ . Therefore  $\epsilon_{out}/\epsilon_{in} = (-2v)/(1-v)$ .

S5. Calculation of in-plane strain of the TiN buffer layer and the Cu top layer in the Cu/TiN/MgO(001) specimen with the Cu top layer grown at 75 °C and the Cu top layer and the TiN buffer layer in the cube-on-cube orientation, based on the Poisson's ratio in the [001] direction of TiN and Cu

A cubic crystal is elastically isotropic in the (001) plane. The Poisson's ratio in the [001] direction of the cubic crystal is  $v_{001} = C_{12}/(C_{11} + C_{12})$  [55]. The elastic stiffness constants of TiN are known:  $C_{11} = 507$  GPa,  $C_{12} = 96$  GPa,  $C_{44} = 163$  GPa [56]. Therefore  $v_{001} = C_{12}/(C_{11} + C_{12}) = 0.159$  for TiN. Based on results shown in Section S4,  $\varepsilon_{out}/\varepsilon_{in} = (-1)[2v/(1-v)] = -0.3781$  for TiN. Data shown in Fig. 8 of the main text show that  $Q_z^{024}(TiN)/[2Q_x^{024}(TiN)] = (1 + \varepsilon_{in})/(1 + \varepsilon_{out}) = 0.9949$ . The in-plane strain for TiN is thus obtained to be  $\varepsilon_{in} = -0.0037$ . The negative sign signals an in-plane compressive strain.

The elastic stiffness constants of Cu are also known:  $C_{11} = 168.4$  GPa,  $C_{12} = 121.4$  GPa,  $C_{44} = 75.4$  GPa [57]. Therefore,  $v_{001} = C_{12}/(C_{11} + C_{12}) = 0.419$  for Cu, and  $\varepsilon_{out}/\varepsilon_{in} = (-1)[2v/(1-v)] = -1.4423$  for Cu. Data shown in Fig. 8 of the main text show that  $Q_z^{204}(Cu)/[2Q_x^{204}(Cu)] = (1 + \varepsilon_{in})/(1 + \varepsilon_{out}) = 1.0074$ . The in-plane strain for Cu is thus obtained to be  $\varepsilon_{in} = +0.003$ . The positive sign signals an in-plane tensile strain.

S6. Calculation of in-plane strain of the TiN buffer layer in the Cu/TiN/MgO(001) specimen with the Cu top layer grown at 105 °C and the Cu top layer and the TiN buffer layer in the new orientation of Cu(110)//TiN(001) in the growth direction, Cu<111>//TiN<100> and Cu<112>//TiN<100> in the growth plane, based on the Poisson's ratio in the [001] direction of TiN

Figure 9(c) in the main text shows RSM data collected around (024) reflections of MgO and TiN. The reciprocal space locations of MgO and TiN (024) peaks,  $(Q_x, Q_z)$ , as listed in Table 2 in the main text, are respectively (0.36551, 0.73175) and (0.36573, 0.72503) in reciprocal lattice units (rlu). The location of the MgO (002) peak is at (-0.00017, 0.36577), again listed in Table 2 in the main text.

Comparing the locations of MgO (002) and (024) peaks obtained from the RSM data, e.g.,  $(Q_z^{002}-Q_x^{024})/Q_x^{024}=0.0007$  and  $(Q_z^{024}-2Q_x^{024})/2Q_x^{024}=-0.0010$ , the cubicity of the MgO substrate is seen to be satisfied to within  $1\times10^{-3}$ . It is then noted that  $Q_z^{024}(TiN)/[2Q_x^{024}(TiN)]=0.9912$ , deviating from cubicity by  $>8\times10^{-3}$  and indicating that the out-of-plane lattice parameter is larger than the in-plane lattice parameter. Again,  $Q_z^{024}(TiN)/[2Q_x^{024}(TiN)]=(1+\varepsilon_{in})/(1+\varepsilon_{out})$ , assuming that this deviation from cubicity is due entirely to the presence of an equal-biaxial in-plane stress. Noting again that  $\varepsilon_{out}=-0.3781\varepsilon_{in}$  for TiN, the in-plane strain for the TiN buffer layer is obtained to be compressive,  $\varepsilon_{in}=-0.0064$ . This calculated  $\varepsilon_{in}$  value is close to the bulk lattice misfit between TiN and MgO,  $\delta=(a_{\text{TiN}}-a_{\text{MgO}})/a_{\text{MgO}}=+0.007$ , suggesting that the TiN buffer layer of this specimen is closer to being fully strained with respect to the MgO(001) substrate.

### **Supplemental Materials References:**

- [1] M.I. Baskes, R.A. Johnson, Modified embedded atom potentials for HCP metals, Model. Simul. Mater. Sci. Eng. 2, 147–163 (1994). https://doi.org/10.1088/0965-0393/2/1/011.
- [2] M.I. Baskes, J.S. Nelson, A.F. Wright, Semiempirical modified embedded-atom potentials for silicon and germanium, Phys. Rev. B. 40, 6085–6100 (1989). https://doi.org/10.1103/PhysRevB.40.6085.
- [3] M.I. Baskes, Modified embedded-atom potentials for cubic materials and impurities, Phys. Rev. B. 46, 2727–2742 (1992). https://doi.org/10.1103/PhysRevB.46.2727.
- [4] B.-J. Lee, J.-H. Shim, M.I. Baskes, Semiempirical atomic potentials for the fcc metals Cu, Ag, Au, Ni, Pd, Pt, Al, and Pb based on first and second nearest-neighbor modified embedded atom method, Phys. Rev. B. 68, 144112 (2003). http://link.aps.org/doi/10.1103/PhysRevB.68.144112.
- [5] B.-J. Lee, M.I. Baskes, H. Kim, Y. Koo Cho, Second nearest-neighbor modified embedded atom method potentials for bcc transition metals, Phys. Rev. B. 64, 184102 (2001). https://doi.org/10.1103/PhysRevB.64.184102.
- [6] B.-J. Lee, M.I. Baskes, Second nearest-neighbor modified embedded-atom-method potential, Phys. Rev. B 62, 8564–8567 (2000). https://doi.org/10.1103/PhysRevB.62.8564.
- [7] Y. Yang, H. Lu, C. Yu, J.M. Chen, First-principles calculations of mechanical properties of TiC and TiN, J. Alloys Compd. 485(1-2), 542–547 (2009). https://doi.org/10.1016/j.jallcom.2009.06.023.
- [8] B.-J. Lee, T.-H. Lee, S.-J. Kim, A modified embedded-atom method interatomic potential for the Fe–N system: A comparative study with the Fe–C system, Acta Mater. 54, 4597–4607 (2006). https://doi.org/10.1016/j.actamat.2006.06.003.
- [9] P. Liu, X. Han, D. Sun, Q. Wang, Development and application of a ternary Ti-Al-N interatomic potential for Ti<sub>2</sub>AlN/TiAl composite, J. Alloys Compd. 745, 63–74 (2018). https://doi.org/10.1016/j.jallcom.2018.02.168.
- [10] C. Wu, B.-J. Lee, X. Su, Modified embedded-atom interatomic potential for Fe-Ni, Cr-Ni and Fe-Cr-Ni systems, Calphad. 57, 98–106 (2017). https://doi.org/10.1016/j.calphad.2017.03.007.

- [11] S. Sun, B.R. Ramachandran, C.D. Wick, Solid, liquid, and interfacial properties of TiAl alloys: parameterization of a new modified embedded atom method model, J. Phys. Condens. Matter. 30, 75002 (2018). https://doi.org/10.1088/1361-648X/aaa52c.
- [12] J.P. Perdew, K. Burke, M. Ernzerhof, Generalized gradient approximation made simple, Phys. Rev. Lett. 77, 3865–3868 (1996). https://doi.org/10.1103/PhysRevLett.77.3865.
- [13] G. Kresse, J. Furthmüller, Efficient iterative schemes for ab initio total-energy calculations using a plane-wave basis set, Phys. Rev. B Condens. Matter Mater. Phys. 54, 11169–11186 (1996). http://www.scopus.com/inward/record.url?eid=2-s2.0-2442537377&partnerID=40&md5=8f0b5e5a94e682d52a2cd379043aa094.
- [14] J. Hafner, Ab-initio simulations of materials using VASP: Density-functional theory and beyond, J. Comput. Chem. 29, 2044–2078 (2008). https://doi.org/10.1002/jcc.21057.
- [15] H.J. Monkhorst, J.D. Pack, Special points for Brillouin-zone integrations, Phys. Rev. B. 13, 5188–5192 (1976). https://doi.org/10.1103/PhysRevB.13.5188.
- [16] A.S.M. Miraz, S. Sun, S. Shao, W.J. Meng, B.R. Ramachandran, C.D. Wick, Computational study of metal/ceramic interfacial adhesion and barriers to shear displacement, Comput. Mater. Sci. 168, 104–115 (2019). https://doi.org/10.1016/j.commatsci.2019.06.006.
- [17] B. Jelinek, S. Groh, M.F. Horstemeyer, J. Houze, S.G. Kim, G.J. Wagner, A. Moitra, M.I. Baskes, Modified embedded atom method potential for Al, Si, Mg, Cu, and Fe alloys, Phys. Rev. B. 85, 245102 (2012). http://link.aps.org/doi/10.1103/PhysRevB.85.245102.
- [18] Y.-M. Kim, B.-J. Lee, Modified embedded-atom method interatomic potentials for the Ti–C and Ti–N binary systems, Acta Mater. 56, 3481–3489 (2008). https://doi.org/10.1016/j.actamat.2008.03.027.
- [19] Y.-M. Kim, B.-J. Lee, M.I. Baskes, Modified embedded-atom method interatomic potentials for Ti and Zr, Phys. Rev. B. 74, 14101 (2006). https://doi.org/10.1103/PhysRevB.74.014101.
- [20] A. Tunde Raji, S. Scandolo, R. Mazzarello, S. Nsengiyumva, M. Härting, D. Thomas Britton, Ab initio pseudopotential study of vacancies and self-interstitials in hcp titanium, Philos. Mag. 89, 1629–1645 (2009). https://doi.org/10.1080/14786430903019032.
- [21] W. Schüle, Properties of vacancies in copper determined by electrical resistivity techniques, Zeitschrift Für Met. 89, 672–677 (1998).

- [22] T. Hehenkamp, W. Berger, J.-E. Kluin, C. Lüdecke, J. Wolff, Equilibrium vacancy concentrations in copper investigated with the absolute technique, Phys. Rev. B. 45, 1998 (1992).
- [23] F.R. de Boer, R. Boom, W.C.M. Mattens, A.R. Miedema, A.K. Niessen, Cohesion in Metals
   Transition Metal Alloys, North-Holland Physics Publishing, Amsterdam, 1988.
- [24] W.R. Tyson, W.A. Miller, Surface free energies of solid metals: estimation from liquid surface tension measurements, Surf. Sci. 62, 267–276 (1977). https://doi.org/10.1016/0039-6028(77)90442-3.
- [25] M.P.J. Punkkinen, Q.-M. Hu, S.K. Kwon, B. Johansson, J. Kollár, L. Vitos, Surface properties of 3d transition metals, Philos. Mag. 91, 3627–3640 (2011). https://doi.org/10.1080/14786435.2011.586953.
- [26] R.B. Ross, Metallic Materials Specification Handbook, Springer US: Boston, MA, 1992. https://doi.org/10.1007/978-1-4615-3482-2.
- [27] E.S. Fisher, C.J. Renken, Single-crystal elastic moduli and the hcp→ bcc transformation in Ti, Zr, and Hf, Phys. Rev. 135, A482 (1964).
- [28] G. Simmons, H. Wang, Single Crystal Elastic Constants and Calculated Aggregate Properties: A Handbook, The MIT Press, 1971. ISBN: 0262190923.
- [29] S.. Epstein, O. Carlson, The elastic constants of nickel-copper alloy single crystals, Acta Metall. 13, 487–491 (1965). https://doi.org/10.1016/0001-6160(65)90098-2.
- [30] W.M. Haynes, CRC Handbook of Chemistry and Physics, CRC press, 2014.
- [31] C. Leyens, M. Peters, eds., Titanium and Titanium Alloys, Wiley, 2003. https://doi.org/10.1002/3527602119.
- [32] L. Ben Freund, S. Suresh, Thin Film Materials Stress, Defect Formation and Surface Evolution, Cambridge University Press, 2004.
- [33] B. Ferdinand, J. DeWolf, E.R. Johnston Jr, D. Mazurek, Mechanics of Materials, McGraw-Hill Education, 2014.
- [34] M. Marlo, V. Milman, Density-functional study of bulk and surface properties of titanium nitride using different exchange-correlation functionals, Phys. Rev. B 62(4), 2899–2907 (2000). https://doi.org/10.1103/PhysRevB.62.2899.
- [35] Y.-M. Kim, B.-J. Lee, A semi-empirical interatomic potential for the Cu–Ti binary system, Mater. Sci. Eng. A. 449–451, 733–736 (2007). https://doi.org/10.1016/j.msea.2006.02.345.

- [36] J.L. Murray, H.A. Wriedt, Phase Diagrams of Binary Titanium Alloys, ed. by JL Murray, ASM Int. Met. Park. OH, USA. 319 (1987) 327.
- [37] J.O. Kim, J.D. Achenbach, P.B. Mirkarimi, M. Shinn, S.A. Barnett, Elastic constants of single-crystal transition-metal nitride films measured by line-focus acoustic microscopy, J. Appl. Phys. 72, 1805–1811 (1992). https://doi.org/10.1063/1.351651.
- [38] R.A. Andrievskii, I.I. Spivak, Handbook of the Strength of Refractory Compounds and Materials Based on Them, Metall. Chelyabinsk Branch, Moscow. (1989).
- [39] S.V. Dudiy, B.I. Lundqvist, Wetting of TiC and TiN by metals, Phys. Rev. B. 69, 125421 (2004). https://doi.org/10.1103/PhysRevB.69.125421.
- [40] W.J. Meng, G.L. Eesley, Growth and mechanical anisotropy of TiN thin films, Thin Solid Films 271(1–2), 108–116 (1995).
- [41] V.N. Eremenko, Y.I. Buyanov, S.B. Prima, Phase diagram of the system titanium-copper, Sov. Powder Metall. Met. Ceram. 5, 494–502 (1966). https://doi.org/10.1007/BF00775543.
- [42] J.L. Murray, The Cu-Ti (Copper-Titanium) system, Bull. Alloy Phase Diagrams. 4, 81–95 (1983). https://doi.org/10.1007/BF02880329.
- [43] K.H.J. Buschow, Thermal stability of amorphous Ti-Cu alloys, Acta Metall. 31, 155–160 (1983). https://doi.org/10.1016/0001-6160(83)90075-5.
- [44] C. Colinet, A. Pasturel, K.H.J. Buschow, Enthalpies of formation of Ti-Cu intermetallic and amorphous phases, J. Alloys Compd. 247, 15–19 (1997). https://doi.org/10.1016/S0925-8388(96)02590-X.
- [45] M. Arita, R. Kinaka, M. Someno, Application of the metalhydrogen equilibration for determining thermodynamic properties in the ti-cu system, Metall. Trans. A. 10, 529–534 (1979). https://doi.org/10.1007/BF02658315.
- [46] U. Zachwieja, H. Jacobs, Ammonothermalsynthese von kupfernitrid, Cu3N, J. Less Common Met. 161, 175–184 (1990). https://doi.org/10.1016/0022-5088(90)90327-G.
- [47] G. Welsch, R. Boyer, E.W. Collings, Materials Properties Handbook: Titanium Alloys, ASM international, 1993.
- [48] Y. Mishin, M.J. Mehl, D.A. Papaconstantopoulos, A.F. Voter, and J.D. Kress, Structural stability and lattice defects in copper: Ab initio, tight-binding, and embedded-atom calculations, Phys. Rev. B 63, 224106 (2001).

- [49] X. Zhang, B. Zhang, Y. Mu, S. Shao, C.D. Wick, B.R. Ramachandran, W.J. Meng, Mechanical failure of metal/ceramic interfacial regions under shear loading, Acta Mater. 138, 224-236 (2017).
- [50] S. Shao, F. Akasheh, J. Wang, Y. Liu, Alternative misfit dislocations pattern in semi-coherent FCC {100} interfaces, Acta Mater. 144, 177-186 (2018).
- [51] M. Dodaran, J. Wang, Y. Chen, W.J. Meng, S. Shao, Energetic, structural and mechanical properties of terraced interfaces, Acta Mater. 171, 92-107 (2019).
- [52] S. Plimpton, Fast Parallel Algorithms for Short-Range Molecular Dynamics, J Comp Phys, 117, 1-19 (1995).
- [53] A. Stukowski, Visualization and analysis of atomistic simulation data with OVITO the Open Visualization Tool, Modelling Simul. Mater. Sci. Eng. 18, 015012 (2010).
- [54] B. Fultz, J. Howe, Transmission Electron Microscopy and Diffractometry of Materials, Springer, Berlin, 2001.
- [55] J.F. Ney, Physical Properties of Crystals, Oxford University Press, Oxford (1985).
- [56] W.J. Meng, G.L. Eesley, Growth and mechanical anisotropy of TIN thin films, Thin Solid Films 27, 108-116 (1995).
- [57] M. Meyers, K. Chawla, Mechanical Behaviors of Materials, 2<sup>nd</sup> edition, Cambridge University Press, Cambridge (2009).